fluids

MDPI

Article

Frequency Variations of Two-Mode Interference Patterns Due to Internal Soliton Waves in Shallow Water

Matthias Ehrhardt [1,*], Sergey Pereselkov [2], Venedikt Kuz'kin [3], Sergey Tkachenko [2] and Alexey Pereselkov [2]

[1] Applied and Computational Mathematics, University of Wuppertal, Gaußstraße 20, 42119 Wuppertal, Germany
[2] Mathematical Physics and Information Technology Department, Voronezh State University, 394018 Voronezh, Russia; pereselkov@yandex.ru (S.P.); tkachenko.edu@yandex.ru (S.T.); pereselkov.edu@yandex.ru (A.P.)
[3] Prokhorov General Physics Institute, Russian Academy of Sciences, 119991 Moscow, Russia; kumiov@yandex.ru
* Correspondence: ehrhardt@uni-wuppertal.de

Abstract

This paper presents a theoretical analysis of frequency shifts in broadband acoustic field interference structures caused by an internal soliton wave in shallow water. It analyzes the spectral signature of interference-maxima frequency shifts within a coupled-mode framework that describes the scattering of acoustic normal modes under soliton-induced perturbations. Using the weak coupling approximation, analytical expressions are obtained for modal phase variations and the spectral peak frequency associated with the temporal evolution of frequency shifts induced by internal soliton waves. The analytical estimates obtained in the weak coupling approximation are extensively validated using numerical simulations under realistic ocean conditions without invoking it. This paper's theoretical analysis demonstrates that internal soliton wave-induced mode coupling produces frequency shift spectrum signatures that strongly depend on soliton parameters. These results suggest that it is potentially feasible to estimate key soliton parameters, such as propagation direction, velocity, and effective amplitude, from measured frequency shifts. Numerical simulations demonstrate the feasibility of solving this inverse problem. These findings highlight the potential of frequency shift analysis as a practical, robust tool for remote sensing of internal wave dynamics in ocean acoustics.

Keywords: internal soliton waves; KdV equation; sound field; mode coupling; interference pattern; frequency shift; shallow water; waveguide

Check for updates

Received: 26 March 2026
Revised: 25 April 2026
Accepted: 26 April 2026
Published: 29 April 2026

Copyright: © 2026 by the authors. Licensee MDPI, Basel, Switzerland. This article is an open access article distributed under the terms and conditions of the Creative Commons Attribution (CC BY) license.

1. Introduction

Research on interference patterns formed by acoustic fields in oceanic waveguides is a fundamental topic in underwater acoustics [1,2]. The spatial–frequency structure of these patterns contains essential information about waveguide properties, source characteristics, and environmental perturbations, thereby motivating interest in the topic. A major advance in interpreting frequency-range striations and related interference effects was achieved through the concept of the waveguide invariant [2], which established a unified framework for analyzing them in both modal and ray-based descriptions [3–6]. Subsequent studies have extended this framework to more realistic and complex scenarios, including range-dependent environments, receiver-depth effects, thermocline influence, and mode coupling [7–12]. More recent investigations have shown that interference structure analysis

can be applied to deep-water waveguides, where the waveguide invariant is more appropriately treated as a distributed rather than constant parameter [10,13]. Taken together, these studies demonstrate that interference patterns are a physically informative tool for acoustic diagnostics and interferometric signal processing, not merely a manifestation of multipath propagation.

In recent years, increasing attention has been paid to interferometric signal processing (ISP) in underwater acoustics because it provides an effective framework for extracting physically meaningful information from broadband acoustic fields in ocean waveguides [14–16]. Several influential studies developed the core theoretical ideas and methodological basis of ISP, defining the principal concepts of this approach and revealing its usefulness for underwater acoustic diagnostics [14–16]. Subsequent work has demonstrated ISP's effectiveness in a wide range of practical applications. In particular, ISP-based techniques have been used to estimate waveguide-invariant parameters [17,18]. These techniques have also been confirmed to be effective in analyzing weak signals, especially when combined with array beamforming to improve signal detectability [19]. Additionally, ISP has been used for seabed characterization based on acoustic emissions from passing ships [20] and for estimating source range in shallow-water environments [21]. A method for range-independent invariant estimation within the ISP framework was introduced in [22], whereas [6] considered the interpretation of interference fringes in terms of eigenray or eigenbeam arrival times. Furthermore, ISP has been adapted for passive sonar applications in deep-water settings [13,23]. Overall, these studies demonstrate that the ISP approach is flexible and provides valuable physical information for analyzing acoustic fields in a wide range of underwater waveguide environments.

Among ISP-based techniques, holographic signal processing (HSP) is one of the most promising directions [24,25]. The underlying physical concepts and mathematical formulation of hologram construction were first introduced in [24]. In the HSP approach, the quasi-coherent integration of acoustic intensity in the frequency–time domain results in the formation of an interferogram. This accumulated intensity distribution is analyzed by applying a classical two-dimensional Fourier transform (2D-FT) [24] or fractional Fourier transform (FrFT) [26] to the interferogram. The resulting quantity is commonly referred to as the Fourier hologram, or simply the hologram. In this representation, the acoustic energy contained in the interferogram is localized into focal regions formed in the hologram domain as a result of the interference of different propagating modes of the sound field. This process is analogous to the spatial focusing of wave fields achieved by wavefront reversal and time-reversal techniques [27], but it does not require extended receiver arrays or occur in the physical space of the waveguide. Instead, focusing occurs in the frequency–time domain of the hologram. HPS is a viable alternative to the traditional matched field processing (MFP) approach [28–32]. Despite its broad use in underwater acoustics, MFP's practical performance depends heavily on precise a priori information about the propagation environment, including detailed descriptions of the water column and seabed characteristics [28,29]. In shallow-water waveguides, however, environmental information is often limited or uncertain. Variability associated with internal waves, tides, and changes in stratification can cause substantial model mismatch, reducing the effectiveness of MFP [30,31]. In contrast, the proposed holographic approach relies less on precise environmental knowledge and remains efficient even when information about the waveguide is incomplete. This makes it a promising tool for adaptive acoustic sensing in complex marine conditions [32].

In the early stages of HSP development, the waveguide was typically considered stationary in space and time. In practice, however, acoustic propagation often occurs in waveguides that are subject to hydrodynamic disturbances. The feasibility of applying HSP

to a stationary source under realistic ocean conditions was first examined in a series of experiments [33–36]. These studies demonstrated that hydrodynamic inhomogeneities deform the interferogram and cause the focal regions in the corresponding hologram to broaden. Under these conditions, the hologram can be interpreted as the sum of two components: one associated with the unperturbed waveguide and one produced by the perturbations. This two-component representation was used in [33–36] to interpret experimental results obtained in the SWARM'95 experiment [37–39]. The waveguide inhomogeneities observed during SWARM'95 were mainly related to internal soliton waves (ISWs), which are among the most common hydrodynamic processes in the ocean [40–42]. Two acoustic tracks were used in the SWARM'95 experiment; both were generated by a single source and recorded by two vertically separated receiving arrays. The first track was oriented at a small angle relative to the ISW front. In this geometry, ISW structures produced strong horizontal refraction of acoustic rays. In a previous study [43], we investigated changes in the hologram structure for a moving source under conditions of pronounced horizontal ray refraction caused by ISWs. In contrast, the second acoustic track in SWARM'95 was directed across the ISW front so that the waves would propagate along the source–receiver path. In this configuration, the dominant effect was not horizontal refraction, but rather, substantial redistribution of acoustic energy between propagating modes, i.e., mode coupling. This mechanism was addressed in our earlier paper [44]. That paper [44] presents a detailed analysis of the influence of ISWs propagating along the acoustic path on the hologram structure of a moving source. Identifying the characteristic features of variations in the source interferogram structure caused by strong ISW-induced mode coupling is essential for further developing HSP. For this reason, the present paper focuses on analyzing this effect.

The primary objective of this work is to develop a theory of frequency shifts in broadband acoustic-field interference structures induced by ISW in shallow water. Kuz'kin and Pereselkov first proposed and developed a theory of frequency shifts of interference maxima in the sound field of inhomogeneous oceanic waveguides [45–49]. This study analyzes the effect of soliton-induced perturbations on frequency shifts of interference maxima within a coupled-mode framework. Particular attention is given to clarifying the relationship between frequency shift signatures and soliton parameters. Within the weak coupling approximation, analytical expressions are derived for modal amplitude and phase variations, as well as for the spectral peak frequency associated with the temporal evolution of frequency shifts induced by ISW. The validity of the analytical estimates is extensively assessed through numerical simulations under realistic ocean conditions without relying on the weak coupling approximation. These analytical and numerical results demonstrate that soliton-induced mode coupling produces pronounced and robust ISW signatures in the frequency-shift spectrum. The characteristics of these signatures depend strongly on soliton parameters, such as propagation direction, velocity, and effective amplitude, as well as on the modal structure of the acoustic field. These spectral features can serve as informative indicators of internal wave dynamics. The findings of this paper indicate the feasibility of estimating key soliton parameters from measured frequency shifts, a notion further supported by numerical simulations. Overall, this study demonstrates the potential of frequency-shift analysis as an effective, robust tool for remote sensing of internal wave dynamics in ocean acoustics.

This study uses numerical modeling to analyze the propagation of sound in three-dimensional (3D) inhomogeneous shallow-water waveguides. Under these conditions, the acoustic field's structure can substantially change due to 3D environmental inhomogeneities caused by internal wave (ISW)-induced scattering. Simulating broadband, low-frequency sound fields in these environments is computationally demanding and typically requires

advanced numerical methods and high-performance computing resources to achieve physically reliable solutions. Existing numerical approaches for simulating sound propagation in inhomogeneous shallow-water waveguides commonly fall into five categories [50]: models based on the 3D Helmholtz equation (3DHE) [51–53]; models based on the 3D parabolic equation (3DPE) [54–60]; three-dimensional ray-based (3DR) models [61–63]; approaches based on vertical modes and the 2D modal parabolic equation (VMMPE) [43,64–67]; and models employing vertically coupled modes with horizontal rays (VCMHR) [68–81].

In this paper, we examine the propagation of low-frequency acoustics in the 90–120 Hz band. We assume that the spatial variability of the shallow-water waveguide is primarily associated with ISWs propagating along the acoustic path between the source and receiver. These ISW-induced inhomogeneities produce significant scattering effects and must therefore be considered in the numerical description of the sound field. Of the five classes of numerical approaches outlined above, the VCMHR model is the most appropriate for this problem. The VCMHR model is specifically suited to low-frequency sound propagation in shallow-water waveguides influenced by ISWs, which is why it is the most appropriate choice for this problem. In particular, the VCMHR model adequately treats the boundary conditions while reproducing the essential physical mechanism of vertical mode coupling caused by environmental inhomogeneity. This feature is especially important for the present study, in which mode coupling plays a central role in the transformation of the acoustic field. Fully three-dimensional models are generally more advantageous for higher-frequency applications but less efficient for describing low-frequency mode-coupling effects in shallow water. The 3DHE and 3DPE approaches can deliver highly accurate solutions, but they are not applicable to the present problem due to the high computational cost of solving a fully 3D propagation problem. VMMPE models are effective at describing horizontal refraction but do not sufficiently represent mode coupling, one of the key mechanisms examined in this work. For these reasons, the VCMHR approach was selected as the most suitable numerical framework for simulating sound propagation in a shallow-water waveguide perturbed by ISWs.

The paper models the shallow-water waveguide as a medium whose spatial and temporal variability is governed by ISWs. The simulations are based on the assumption that the speed of an acoustic wave ($\sim$1500 m/s) is significantly higher than the speed at which ISWs propagate ($\sim$0.5–1 m/s). This difference in characteristic velocities justifies the use of the "frozen environment" approximation [63,82], in which the medium is assumed to remain effectively unchanged during acoustic propagation between the source and receiver.

The paper is organized as follows. Section 1 provides the introduction. Section 2 describes the three-dimensional model of a shallow-water waveguide in the presence of ISWs propagating along the acoustic path. In Section 3 develops the theory of frequency shifts for the two-mode case. Section 4 presents the numerical results for the frequency shifts of a broadband sound source in a shallow-water waveguide under conditions of significant ISW-induced mode coupling. Section 5 considers the inverse problem of estimating ISW parameters and demonstrates the possibility of addressing it using information on frequency shifts within a numerical modeling framework. The main conclusions are presented in Section 6. Section 7 describes the next phase of our research.

2. The Shallow Water Waveguide Model

This section introduces a three-dimensional description of the shallow-water acoustic waveguide considered in this work (see Figure 1). The model is formulated in a Cartesian coordinate system (X, Y, Z). The propagation medium is represented by a water layer whose acoustic properties are characterized by a sound speed $c(\mathbf{r}, z, t)$ and a density $\rho(\mathbf{r}, z, t)$, that vary in both space and time. The horizontal location is specified by the vector $\mathbf{r} = (x, y)$.

The upper boundary of the domain corresponds to the sea surface located at $z = 0$, and the lower boundary is formed by the ocean bottom at depth $z = H$. The seabed is described by the density parameter ρ_b and by a complex refractive index of the form $n_b(1 + \mathrm{i}\varkappa)$ [63,82]. The quantity $\varkappa$ accounts for acoustic attenuation within the bottom medium and is given by $\varkappa = \chi c_b/(54.6f)$. In this equation, the bottom loss coefficient is denoted by χ, the sound speed in the bottom material is denoted by c_b and the acoustic frequency is denoted by f.

The spatial and temporal variability of the acoustic properties of the water column can be represented as follows [63,82]:

$$c(\mathbf{r}, z, t) = \bar{c}(z) + \tilde{c}(\mathbf{r}, z, t), \tag{1}$$

where $\bar{c}(z)$ denotes the reference sound-speed profile characterizing the medium when internal wave processes are absent. The term $\tilde{c}(\mathbf{r}, z, t)$ represents the fluctuations of the sound speed caused by the presence of internal soliton waves (ISWs).

Using Equation (1), the square of the refractive index within the water column can be written as [63,82]:

$$n^2(\mathbf{r}, z, t) = \bar{n}^2(z) + \tilde{n}^2(\mathbf{r}, z, t), \tag{2}$$

where $\bar{n}^2(z)$ represents the background refractive-index distribution corresponding to the undisturbed medium and $\tilde{n}^2(\mathbf{r}, z, t)$ describes the variation produced by ISWs. According to the approach presented in [42,64], the perturbation term can be expressed as

$$\tilde{n}^2(\mathbf{r}, z, t) = -2QN^2(z)\hat{\Phi}(z)\zeta(\mathbf{r}, t), \tag{3}$$

where $Q \approx 2.4\ \mathrm{s}^2/\mathrm{m}$ is a constant that depends on the physical properties of seawater. The quantity $N(z) = \left(-\frac{g}{\rho}\frac{d\rho}{dz}\right)^{1/2}$ denotes the buoyancy (Brunt–Väisälä) frequency, $\hat{\Phi}(z)$ is the eigenfunction of the first internal gravity mode, normalized to unity at termocline depth, and $\zeta(\mathbf{r}, t)$ characterizes the vertical displacement of termocline water layer generated by ISWs.

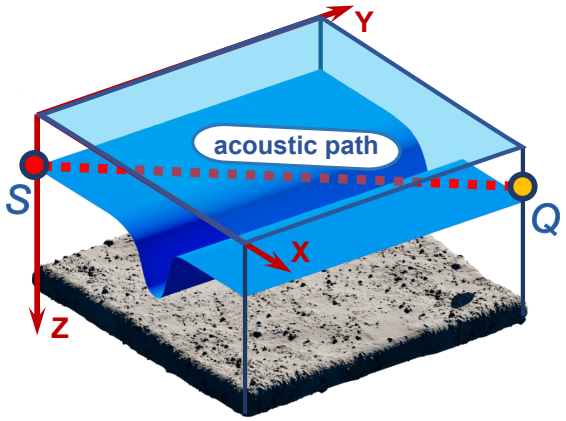


Figure 1. Model of a shallow water waveguide at presence of ISWs: *S*—source, *Q*—receiver, dashed line—source–receiver path.

ISWs are commonly observed in oceanic environments. They appear as sequences of short-period vertical oscillations of stratified water layers and can be interpreted as packets of internal solitary waves that propagate toward the continental shelf. ISW generation is typically associated with internal tidal processes [40–42]. Representative characteristics of these waves, obtained from experimental observations, are summarized in Table 1 [37,38,40–42]. These parameters give rise to distinct acoustic effects in the marine environment.

According to the reported results [64], when ISWs intersect the acoustic track between a source and a receiver, they significantly impact the horizontal refraction of acoustic rays propagating at small angles relative to the wavefronts of the internal waves. Consequently, time-dependent horizontal waveguides are formed, whose axes are oriented approximately parallel to the ISW fronts. We analyzed the influence of this phenomenon on the holographic pattern produced by a moving acoustic source in our earlier works, for example, [43]. In contrast, when ISWs propagate along the acoustic path between the source and receiver, pronounced coupling occurs between acoustic normal modes [44]. This mode coupling redistributes acoustic energy among the modes and modifies the relative amplitudes that determine the structure of the resulting sound field.

Table 1. ISW Parameters.

Parameter	Value
ISW amplitude	$A \sim 10$–30 m
ISW half-width	$L \sim 100$–200 m
ISW velocity	$v \sim 0.5$–1 m/s
ISW curvature radius	$R \sim 15$–25 km

The vertical displacement of fluid parcels caused by a soliton can be described by the Korteweg–de Vries (KdV) equation, where the displacement field takes the form [42,64]:

$$\zeta(x) = A \ \mathrm{sech}^2\left(\frac{x - vt}{L}\right), \tag{4}$$

where A is the soliton amplitude and L characterizes its half-width at the level of 0.42 of the maximum value.

For analytical convenience, this profile (4) is approximated by a rectangular pulse:

$$\zeta(x) = A \ \mathrm{rect}\left(\frac{x}{L}\right) = \begin{cases} A, & |x/L| \leq 1, \\ 0, & |x/L| > 1. \end{cases} \tag{5}$$

This approximation (5) is based on the assumption that the excitation energies of the original and simplified pulses are identical. Accordingly, the areas under the two profiles are considered equal:

$$A \int_{-\infty}^{\infty} \mathrm{sech}^2\left(\frac{x}{L}\right) dx = A \int_{-L}^{L} \mathrm{rect}\left(\frac{x}{L}\right) dx = 2AL. \tag{6}$$

This substitution allows us to disregard the variation in scattering characteristics within the inhomogeneous region.

Figure 2 illustrates the two idealized initial ISW shapes considered in the Equations (4) and (5). Figure 2a shows a squared hyperbolic secant profile representing the KdV solution for an ISW, with a maximum displacement of $A = 15$ m at the ISW crest and a gradual decay toward zero away from the ISW crest. Figure 2b presents an approximate rectangular profile with the same amplitude, $A = 15$ m, characterized by a uniform displacement within the central region and sharp transitions at the ISW edges. The parameter L is 100 m for both profiles.

The adequacy of this theoretical model was verified through numerical simulations of frequency-shift processes in Section 4 in these two representative cases. The modeling was carried out using the following parameters (see Table 2). The undisturbed sound-speed profile versus depth with thermocline is shown in Figure 3. The bottom parameters were set as follows: the ratio of bottom sediment density to water density $\rho_b/\rho = 1.8$, and the

complex refractive index $n_b = 0.82\,(1 + \mathrm{i}\,0.01)$. In the frequency range of 90–120 Hz, modal groups with nearly identical amplitudes were studied, with a spectral discretization of $\delta f = 0.2$ Hz. The acoustic source and receiver were located at a depth of $z_0 = 30$ m, and the horizontal propagation distance was $r_0 = 10$ km.

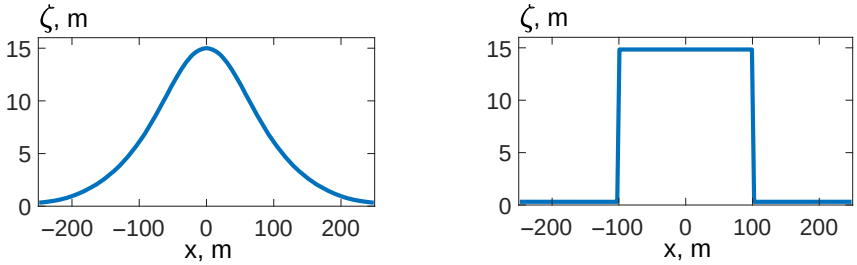


Figure 2. ISW shape: (**a**) squared hyperbolic secant (KdV solution) shape; (**b**) approximate rectangular shape. ISW parameters: $A = 15$ m, $L = 100$ m.

Table 2. Shallow Water Waveguide Parameters.

Parameter	Value
Waveguide depth	70 m
Bottom refractive index	$n_b = 0.82\,(1 + \mathrm{i}\,0.01)$
Bottom density	$\rho_b = 1.8\,\mathrm{g/cm^3}$
Modes count	$M = 2$
Source depth	$z_0 = 30$ m
Receiver depth	$z_0 = 30$ m
Source–receiver range	$r_0 = 10$ km
Frequency band	$\Delta f = 90$–120 Hz

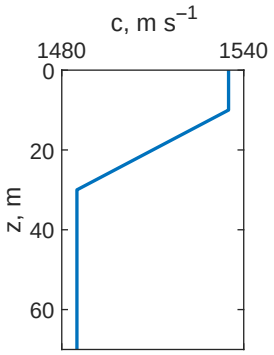


Figure 3. Sound speed dependence in a shallow water waveguide in the absence of ISWs.

The soliton was modeled as a squared hyperbolic secant pulse with the following parameters: amplitude $A = 15$ m, half-width $L = 100$ m, and velocity $v = 1$ m/s.

Figure 4 shows the spatial variations of the sound-speed perturbation $\tilde{c}(x, z)$ associated with two idealized ISW profiles and for undisturbed sound-speed profile shown in Figure 3. In Figure 4a, corresponding to the squared hyperbolic secant KdV solution shape for ISW, the perturbation field is smoothly distributed around the wave core, with the largest values concentrated in the upper part of the domain near the wave center and a gradual decay in both the horizontal and vertical directions. In contrast, Figure 4b displays the perturbation field generated by the approximate rectangular ISW profile, where the region of elevated $\tilde{c}(x, z)$ is more horizontally uniform and confined, with comparatively sharp boundaries at the wave edges.

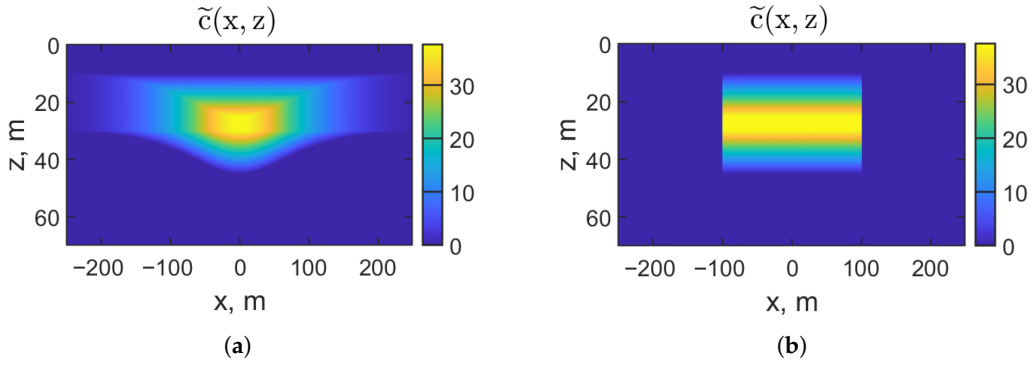


Figure 4. Space variations of the sound speed $\tilde{c}(x, z)$ due to ISW: (**a**) squared hyperbolic secant (KdV solution) shape; (**b**) approximate rectangular shape. ISW parameters: $A = 15\,\text{m}$, $L = 100\,\text{m}$.

The coupling between the first and second modes of the acoustic field ($m = 1$, $n = 2$) was analyzed because this pair exhibits the strongest coupling. To track frequency shift dynamics, a narrow-band local source with a known spectral position within the given frequency band was used.

3. Frequency Shifts Theory: Two-Mode Case

This section presents the theory of frequency shifts for a sound field consisting of two modes. The section is divided into four parts. Section 3.1 describes a sound field consisting of two modes in a shallow-water waveguide in the presence of ISW. Section 3.2 examines the coupled modes approximation for frequency shifts. Section 3.3 considers the case when the ISW propagates along the source–receiver path (case: $\alpha = 0$). Section 3.4 considers the case when the ISW propagates at an angle to the source–receiver path (case: $\alpha \neq 0$).

Figure 5 shows the schematic geometry considered in this study. The source and receiver are denoted by S and Q, respectively. The red dashed line corresponds to the source–receiver path, and the blue dashed vertical line marks the crest of the ISW. The blue arrow indicates the ISW's propagation velocity vector. The angle α is measured between the source–receiver path and the X-axis. In the absence of ISWs, the shallow water waveguide is assumed to be horizontally homogeneous. The width of the ISW front exceeds the length of the source–receiver path. Frequency shifts are analyzed using the quasi-stationary approximation, in which scattering by inhomogeneities occurs as if the perturbation were frozen in time, and the temporal dependence is restored later in the final expressions.

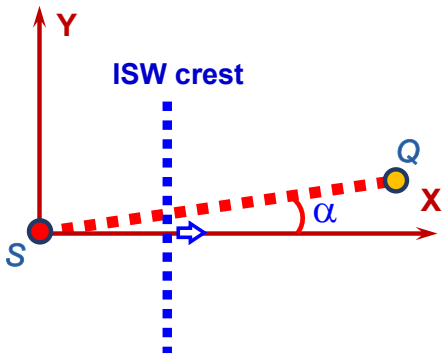


Figure 5. Geometry of the problem: S—source; Q—receiver; red dashed line—source–receiver path; blue dashed line—ISW crest; blue arrow—ISW velocity vector **v**; angle between source–receiver path and X-axis.

3.1. Sound Field Model in the Presence of ISW

Within the framework of the vertical-mode and horizontal-ray approximations, the sound field represented by two modes can be written as follows [63,82]:

$$p(\mathbf{r}, z) = P_m(\mathbf{r})\phi_m(z) + P_n(\mathbf{r})\phi_n(z). \tag{7}$$

Here, $\mathbf{r} = (x, y)$ is the horizontal position vector, P_m and P_n are the modal amplitudes, and $\phi_m(z)$ and $\phi_n(z)$ describe the vertical structure (mode shapes) of the corresponding acoustic modes in an unperturbed waveguide, i.e., in the absence of an ISW. The complex horizontal wavenumber of each mode is defined as $\xi_m = h_m + \mathrm{i}\gamma_m$, where h_m and γ_m denote its real and imaginary parts, respectively. Consequently, the acoustic pressure field p depends on the angular frequency $\omega = 2\pi f$ and wavenumber $k = \omega/c$.

The eigenfunctions $\phi_m(z)$ and the complex wavenumbers h_m are determined by solving the corresponding Sturm–Liouville eigenvalue problem subject to boundary conditions at the free surface and the bottom [63,82]:

$$\frac{d^2\phi_m(z)}{dz^2} + k^2\bar{n}^2(z)\,\phi_m(z) = \xi_m^2\phi_m(z), \tag{8}$$

$$\phi_m(z)\big|_{z=0} = 0, \qquad \phi_m(z)\big|_{z=H} + g(\xi_m)\frac{d\phi_m(z)}{dz}\Big|_{z=H} = 0, \tag{9}$$

where

$$g(\xi_m) = \eta \Big/ \sqrt{\xi_m^2 - k^2 n_b^2(1 + \mathrm{i}\varkappa)}. \tag{10}$$

We will use the coupled mode approach to account for the scattering of the sound field Equation (7) induced by the inhomogeneities of the water layer caused by ISWs. In the mode amplitude $P_m(\mathbf{r})$, we isolate the factor corresponding to cylindrical spreading:

$$P_m(\mathbf{r}) = \frac{M_m(\mathbf{r})}{\sqrt{h_m r}}, \tag{11}$$

where $M_m(\mathbf{r}) = M_m(r, \alpha)$ denotes the mode amplitude without the cylindrical spreading factor. The horizontal range between the source and receiver is r. This representation explicitly factors out the geometric spreading term $1/\sqrt{r}$, which dominates the range dependence in the shallow water waveguide under consideration. For two coupled modes with indices m and n, the system of equations for the complex amplitudes can be written as follows [63,82]:

$$\begin{cases} \dfrac{dM_m(r,\alpha)}{dr} = \mathrm{i}\mu_{mm}(r,\alpha)\,M_m(r,\alpha) + \mathrm{i}\mu_{mn}(r,\alpha)\,M_n(r,\alpha)\,\exp\left(\mathrm{i}h_{nm}r\right), \\ \dfrac{dM_n(r,\alpha)}{dr} = \mathrm{i}\mu_{nn}(r,\alpha)\,M_n(r,\alpha) + \mathrm{i}\mu_{nm}(r,\alpha)\,M_m(r,\alpha)\,\exp\left(\mathrm{i}h_{mn}r\right), \end{cases} \tag{12}$$

where h_m is the unperturbed value of the real part of the horizontal wavenumber for the m-th mode, $h_{mn} = h_m - h_n$, and μ_{mn} represents the mode coupling coefficient, which is determined by the characteristics of the inhomogeneity. The term describing modal attenuation is omitted here, since numerical simulations indicate that it has no significant effect on the subsequent analysis.

In the case of solitonic inhomogeneities, the coupling coefficients are expressed as:

$$\mu_{mn}(r,\alpha) = -\frac{k^2}{2\sqrt{h_m h_n}}\int_0^H \phi_m(z)\,\phi_n(z)\,\tilde{n}^2(r,\alpha,z)\,dz. \tag{13}$$

Equations (12) are symmetric with respect to the interchange of lower indices ($m \leftrightarrow n$), so only the first one will be considered further. When the mode indices are identical ($m = n$), the coefficient μ_{mm} equals the linear correction $\tilde{h}_m$ to the unperturbed wavenumber h_m of the m-th mode ($\mu_{mm} = \tilde{h}_m$). For $m \neq n$, we have that $\mu_{mn} = \mu_{nm}$. We use the expression for the perturbation of the squared refractive index $\tilde{n}^2(r, \alpha, z)$ in the form:

$$\tilde{n}^2(r, \alpha, z) = -2QN^2(z)\,\hat{\Phi}(z)\,\zeta(r, \alpha), \tag{14}$$

and thus, we can rewrite Equation (13) as

$$\mu_{mn}(r, \alpha) = q_{mn}\,\zeta(r, \alpha), \tag{15}$$

where $\zeta(r, \alpha)$ represents the ISW perturbation function varying in space and time (see Equations (4) and (5)). Continuing from Equation (15), we define the coefficient q_{mn} as

$$q_{mn} = \frac{Qk^2}{\sqrt{h_m h_n}} \int_0^H \phi_m(z)\,\phi_n(z)\,N^2(z)\,\hat{\Phi}(z)\,dz. \tag{16}$$

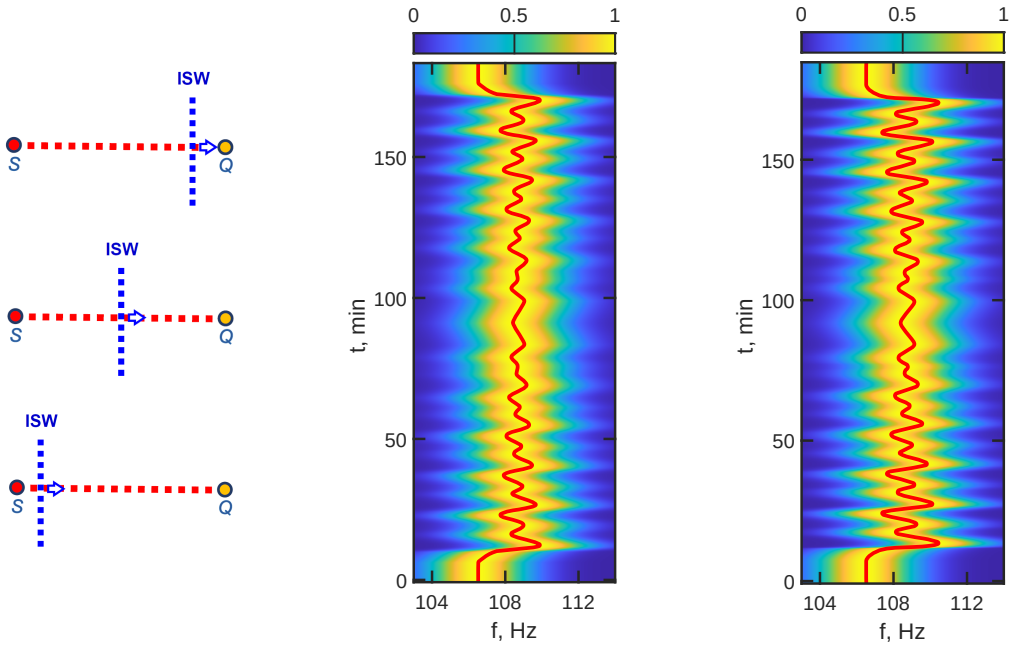
Figure 6 demonstrates how the propagation of an ISW along the source–receiver path results in the time-dependent restructuring of the acoustic interference pattern. Figure 6a presents a schematic of three characteristic ISW positions relative to the fixed source S and receiver Q. These ISW positions correspond to three time points: $t = 25$ min; $t = 95$ min; $t = 165$ min. As the ISW moves along the source–receiver path, it changes the phase relationships among the acoustic modes contributing to the received field, thereby altering the interference structure of the sound intensity in the frequency domain. Consequently, the positions of the interference maxima in the frequency spectrum become time-dependent at the receiver Q. The corresponding evolution of the interference structure in the frequency–time domain is shown in Figure 6b,c. In both cases, the background color maps display alternating high- and low-intensity bands associated with constructive and destructive interference. A key feature of these distributions is their gradual displacement along the frequency axis as time increases. This behavior indicates that the characteristic interference frequencies are not fixed, but vary in response to the ISW motion. The red curve traces the temporal evolution of one of the interference maxima, revealing a pronounced oscillatory frequency shift induced by the moving ISW. The frequency shift value $\Omega(t)$ is defined as the difference between the frequency of the interference maximum at a given time $f(t)$ and the frequency of the interference maximum in the absence of an ISW f_0:

$$\Omega(t) = f(t) - f_0. \tag{17}$$

where $\Omega(t)$ is the frequency shift value, $f(t)$ is the frequency of the interference maximum at time t, and f_0 is the frequency of the interference maximum in the absence of an ISW.

Comparing Figures 6b and 6c shows that both ISW representations produce the same general physical effect. In both cases, the interference pattern undergoes smooth, non-monotonic frequency variations throughout the entire observation interval. The two models remain qualitatively and quantitatively consistent and yield nearly identical temporal signatures of the interference maximum frequency variations.

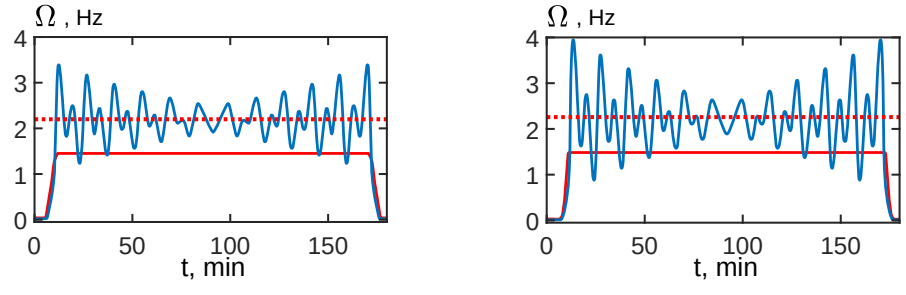
Thus, Figure 6 confirms that ISW motion manifests as measurable frequency shifts of interference fringes in the received acoustic field. These results suggest that the observed spectral variability is determined not only by the presence of the wave itself, but also by its instantaneous position. Therefore, tracking the interference maxima in the frequency–time representation could be a useful tool for diagnosing ISW-induced perturbations and for estimating ISW parameters.



(**a**) (**b**) (**c**)

Figure 6. Frequency shifts due to ISW. (**a**) Scheme of ISW propagation along the source–receiver path. ISW positions at three time moments: $t = 25$ min; $t = 95$ min; $t = 165$. Variations of sound intensity distribution in the frequency-time domain due to ISW motion. (**b**) Squared hyperbolic secant (KdV solution) shape. (**c**) Approximate rectangular shape. ISW parameters: $A = 15$ m, $L = 100$ m, $L = 100$ m, $v = 1$ m/s, $\alpha = 0°$. Red line—variation in the frequency position of interference maxima due to ISW motion.

Figure 7 presents the temporal behavior of the frequency shift $\Omega(t)$ (Equation (17)) produced by the passage of an ISW for two different representations of the inhomogeneity profile. Figure 7a corresponds to the sech^2-type KdV solution, whereas Figure 7b shows the result obtained for the approximate rectangular shape. In both cases, the frequency shift exhibits a pronounced oscillatory behavior superimposed on a nearly constant mean level while the ISW is on the source–receiver path. Outside this interval, $\Omega(t)$ rapidly decreases to values close to zero, reflecting the disappearance of the ISW's perturbing influence on the propagation conditions.



(**a**) (**b**)

Figure 7. Frequency shifts $\Omega(t)$ due to ISW: (**a**) squared hyperbolic secant (KdV solution) shape; (**b**) approximate rectangular shape. Red dotted line—mean value of $\Omega(t)$. Red solid line—$\Omega(t)$ without mode coupling. ISW parameters: $A = 15$ m, $L = 100$ m, $v = 1$ m/s, $\alpha = 0$.

Comparing Figures 7a and 7b shows that the two modeled wave shapes produce nearly identical temporal signatures of the frequency shift. The duration of the disturbed interval, the mean level of $\Omega(t)$, the amplitude of the oscillations, and the overall envelope

of the signal remain nearly unchanged between the two representations. There are only very minor differences in the fine details of the individual oscillations, but the general structure of the curves is accurately preserved. Thus, the time dependence of the frequency shift $\Omega(t)$ is primarily determined by the ISW parameters (amplitude A, velocity v, and half-width L), rather than by subtle differences in its profile shape.

This result is important for the subsequent theoretical analysis. The close agreement between the two cases shows that the simplified, approximate rectangular model accurately captures the essential temporal and spectral characteristics of the more realistic sech^2-type ISW with sufficient accuracy. Therefore, using the approximate rectangular shape is justified in the analysis of frequency shifts. This simplification clarifies the theoretical treatment presented in Sections 3.2–3.4, while preserving the key physical effects associated with ISW-induced frequency shifts $\Omega(t)$.

3.2. Coupled Modes Approximation for Frequency Shifts

Now, let us consider the theory of frequency shift due to the ISW within the framework of the coupled modes approximation. The solution to system (Equation (12)) determines the complex amplitudes of modes M_m and M_n, which can be expressed as

$$\begin{cases} M_m = M_{m0} + \delta M_m, \\ M_n = M_{n0} + \delta M_n, \end{cases} \tag{18}$$

where M_{m0} and M_{n0} are the initial values of the mode amplitudes in the absence of ISW, and δM_m, δM_n are the amplitude perturbations caused by ISW (Equation (5)). For a point source located at a depth z_0, the quantities M_{m0} and M_{n0} are proportional to the mode eigenfunctions $\phi_m(z_0)$ and $\phi_n(z_0)$, up to a constant factor. The expression for the complex phase Θ_m of the mode amplitude M_m cannot be obtained explicitly for the general case. However, for practical purposes, it is convenient to consider the case of weak coupling, when the relative amplitude perturbations $\psi_m = \delta M_m / M_{m0}$ satisfy $|\psi_m| \ll 1$, and the problem can be solved analytically. We introduce the logarithm of the complex mode amplitude M_m. Its imaginary part corresponds to the phase shift of the modal amplitude, and its real part represents the logarithm of its magnitude. Expanding $\ln M_m$ into a power series in terms of the small parameter ψ_m, the modal phase Θ_m can be expressed as a series:

$$\Theta_m = \operatorname{Im} \psi_m - \frac{1}{2} \operatorname{Im} \psi_m^2 + \frac{1}{3} \operatorname{Im} \psi_m^3 + \ldots = \Theta_m^{(0)} + \Theta_m^{(1)} + \Theta_m^{(2)} + \ldots. \tag{19}$$

The first term $\Theta_m^{(0)}$ of this expansion represents the linear approximation to the phase perturbation. The subsequent terms $\Theta_m^{(1)}$, $\Theta_m^{(2)}$, etc., describe higher-order (nonlinear) corrections. The frequency shift Ω_{mn} associated with the coupling of the m-th and n-th modes can then be written as:

$$\Omega_{mn} = \frac{d}{dt}(\Theta_m - \Theta_n). \tag{20}$$

This formulation establishes the connection between modal phase perturbations and observable frequency shifts in the interference pattern. This connection forms the theoretical basis for estimating the characteristics of oceanic inhomogeneities through modal interaction analysis.

$$\Omega_{mn}(r, \alpha) = -\frac{\Theta_{mn}(r, \alpha, f_0)}{G_{mn}}, \quad 0 \le r \le r_0, \tag{21}$$

where $(G_{mn})^{-1} = \left\{ r_0 \left[dh_{mn}(f_0)/d\omega \right] \right\}^{-1}$ is the frequency scale of field variability at distance r_0, determined by modal interference; f_0 is the frequency position of the observed

interference maximum in the absence of ISW; and $\Theta_{mn} = \Theta_m - \Theta_n$ is the phase difference between the modes. Using the definition of the group velocity for the m-th mode, $v_{gm} = d\omega/dh_m$, the coefficient G_{mn} can be written as $G_{mn} = t_{mn}$, where $t_{mn} = t_m - t_n$ represents the time delay between pulses of modes m and n, with $t_m = r_0/v_{gm}$. Thus, Equation (21) shows that phase variations induced by environmental perturbations can be equivalently interpreted in terms of frequency shifts. In particular, the modal phase increment Θ_{mn} can be expressed in terms of the frequency shift Ω_{mn} as $\Theta_{mn} = -t_{mn}\Omega_{mn}$. In other words, frequency shift measurements can serve as indirect phase measurements and can be used effectively in interferometric systems for diagnostic and monitoring purposes.

The solution to Equation (12) can be obtained using the integral method with a second-order approximation. For most practical applications, this approximation is accurate enough to study the influence of oceanic inhomogeneities.

3.3. ISW Propagates Along the Source–Receiver Path: Case $\alpha = 0$

This case corresponds to an angle $\alpha = 0$ (see Figure 5). Substituting the mode amplitudes M_m and M_n with their initial values M_{m0} and M_{n0} into the right-hand side of the Equation (12) and integrating, we obtain

$$M_m(r) = M_{m0} + \mathrm{i}\Big[M_{m0}\int_0^r \mu_{mm}(r')\,dr' + M_{n0}\int_0^r \mu_{mn}(r')\,\exp(\mathrm{i}h_{mn}r')\,dr'\Big]. \tag{22}$$

Performing the second iteration, we obtain:

$$\begin{aligned} M_m(r) = M_{m0} + \Big\{ &- \Big[M_{m0}\int_0^r\int_0^s \mu_{mm}(s)\mu_{mm}(\sigma)\,d\sigma\,ds \\ &+ M_{n0}\int_0^r\int_0^s \mu_{mn}(s)\mu_{mn}(\sigma)\,\mathrm{e}^{\mathrm{i}h_{mn}\sigma}\,d\sigma\,ds\Big] \\ &+ M_{n0}\int_0^r\int_0^s \mu_{mn}(s)e^{\mathrm{i}h_{mn}s}\mu_{mn}(\sigma)\,\mathrm{e}^{\mathrm{i}h_{mn}\sigma}\,d\sigma\,ds \\ &+ M_{m0}\int_0^r\int_0^s \mu_{mm}(s)\mu_{mm}(\sigma)\,\mathrm{e}^{\mathrm{i}h_{mn}\sigma}\,d\sigma\,ds \\ &+ \mathrm{i}\Big[M_{m0}\int_0^r \mu_{mm}(s)\,ds + M_{n0}\int_0^r \mu_{mn}(s)\,\mathrm{e}^{\mathrm{i}h_{mn}s}\,ds\Big]\Big\}. \end{aligned} \tag{23}$$

As can be seen, the first-order solution compared with the second-order one underestimates the increment of the complex amplitude δM_m extracted in Equations (22) and (23) from the expressions within the curly brackets. To determine the complex amplitude, it is sufficient to substitute lower indices $m \to n$ in Equations (22) and (23).

Using Equations (18) and (23), we can isolate the phase increment Θ_m and substitute it into Equation (19), by restricting ourselves to the first two terms. Using Equations (5), (15) and (16) the integration yields an expression for the phase increment Θ_m. Similarly, we can obtain the phase increment Θ_n. Then, accurate to quadratic terms, the expression for the phase difference Θ_{mn}, when transformed to the temporal dependence $t = r/v$, can be written as

$$\begin{gathered} \Theta_{mn}(t) = \bar{\Theta}_{mn} + \hat{\Theta}_{mn}(t), \quad t_1 \le t \le t_2, \\ t_1 = \frac{2L}{v}, \qquad t_2 = \frac{r_0 - 2L}{v}, \end{gathered} \tag{24}$$

where $\bar{\Theta}_{mn}$ is the stationary component of the phase difference, $\hat{\Theta}_{mn}(t)$ represents the oscillating component of the phase difference.

The stationary component of the phase difference $\bar{\Theta}_{mn}$ is defined by the following expression:

$$\bar{\Theta}_{mn} = J_1 + J_2 + J_3 + J_4. \tag{25}$$

In this context, the quantities J_i represent the following constant:

$$
\begin{aligned}
J_1 &= 2AL(q_{mn} - q_{nn}),\\
J_2 &= 4(AL)^3(q_{mn}^3 - q_{nn}^3),\\
J_3 &= 2(AL)^3 q_{mn}^2 \frac{\sin^2(\varphi_{mn})}{\varphi_{mn}^2}\,(q_{mn} - q_{nn}),\\
J_4 &= 2(AL)^3 q_{mn}^2 \frac{\sin^2(\varphi_{mn})}{\varphi_{mn}^2}\left\{(q_{mm} + q_{nn})\left[\left(\frac{M_{n0}}{M_{m0}}\right)^2 - \left(\frac{M_{m0}}{M_{n0}}\right)^2\right]\right\}.
\end{aligned}
\tag{26}
$$

The oscillating component of the phase difference $\hat{\Theta}_{mn}(t)$ is defined by the expression:

$$
\begin{aligned}
\hat{\Theta}_{mn}(t) = {} & I_1 \cos(\omega_{mn}t + \varphi_{mn}) + I_2 \sin(\omega_{mn}t)\\
& + I_3 \sin(\omega_{mn}t + \varphi_{mn}) + I_4 \sin(\omega_{mn}t + 2\varphi_{mn})\\
& + I_5 \sin(2\omega_{mn}t + \varphi_{mn}) + I_6 \sin(2\omega_{mn}t + 2\varphi_{mn})\\
& + I_7 \sin(2\omega_{mn}t + 3\varphi_{mn}) + I_8 \sin(3\omega_{mn}t + 2\varphi_{mn})\\
& + I_9 \sin(3\omega_{mn}t + 3\varphi_{mn}).
\end{aligned}
\tag{27}
$$

Here, the quantities I_i denote the following constants:

$$
\begin{aligned}
I_1 &= 2ALq_{mn}\frac{\sin(\varphi_{mn})}{\varphi_{mn}}\left[\left(\frac{M_{n0}}{M_{m0}} - \frac{M_{m0}}{M_{n0}}\right) + 2(AL)^2\left(q_{mm}^2\frac{M_{n0}}{M_{m0}} - q_{nn}^2\frac{M_{m0}}{M_{n0}}\right)\right.\\
&\quad \left. + (ALq_{mn})^2\frac{\sin^2(\varphi_{mn})}{\varphi_{mn}^2}\left(\frac{M_{n0}}{M_{m0}} - \frac{M_{m0}}{M_{n0}}\right)\right],\\
I_2 &= \frac{A^3L^3q_{mn}}{\varphi_{mn}}\left[q_{mn}^2\frac{\sin^2(\varphi_{mn})}{\varphi_{mn}^2}\left(\frac{M_{n0}}{M_{m0}} - \frac{M_{m0}}{M_{n0}}\right) - 4\left(q_{mm}^2\frac{M_{n0}}{M_{m0}} - q_{nn}^2\frac{M_{m0}}{M_{n0}}\right)\right],\\
I_3 &= \frac{A^3L^3q_{mn}}{\varphi_{mn}}\frac{\sin(\varphi_{mn})}{\varphi_{mn}}\left[4\left(q_{mm}^2\frac{M_{n0}}{M_{m0}} - q_{nn}^2\frac{M_{m0}}{M_{n0}}\right)\right.\\
&\quad \left. + \left(q_{mn}^2\frac{\sin(2\varphi_{mn})}{2\varphi_{mn}} - 4q_{mm}q_{nn}\right)\left(\frac{M_{n0}}{M_{m0}} - \frac{M_{m0}}{M_{n0}}\right)\right],\\
I_4 &= \frac{4A^3L^3q_{mm}q_{nn}q_{mn}}{\varphi_{mn}}\left(\frac{M_{n0}}{M_{m0}} - \frac{M_{m0}}{M_{n0}}\right),\\
I_5 &= -\frac{2A^3L^3q_{mn}^2}{\varphi_{mn}}\frac{\sin(\varphi_{mn})}{\varphi_{mn}}\left\{(q_{mm} - q_{nn}) + \left[q_{mm}\left(\frac{M_{n0}}{M_{m0}}\right)^2 - q_{nn}\left(\frac{M_{m0}}{M_{n0}}\right)^2\right]\right\},\\
I_6 &= \frac{2A^3L^3q_{mn}^2}{\varphi_{mn}}(q_{mm} - q_{nn})\left\{\frac{\sin(2\varphi_{mn})}{2\varphi_{mn}} + \frac{\sin^2(\varphi_{mn})}{\varphi_{mn}^2}\left[\left(\frac{M_{n0}}{M_{m0}}\right)^2 + \left(\frac{M_{m0}}{M_{n0}}\right)^2\right]\right\},\\
I_7 &= \frac{2A^3L^3q_{mn}^2}{\varphi_{mn}}\frac{\sin(\varphi_{mn})}{\varphi_{mn}}\left[q_{nn}\left(\frac{M_{n0}}{M_{m0}}\right)^2 - q_{mm}\left(\frac{M_{m0}}{M_{n0}}\right)^2\right],\\
I_8 &= \frac{A^3L^3q_{mn}^3}{\varphi_{mn}}\frac{\sin^2(\varphi_{mn})}{\varphi_{mn}^2}\left(\frac{M_{n0}}{M_{m0}} - \frac{M_{m0}}{M_{n0}}\right),\\
I_9 &= \frac{A^3L^3q_{mn}^3}{\varphi_{mn}}\frac{\sin(\varphi_{mn})}{\varphi_{mn}}\frac{\sin(2\varphi_{mn})}{2\varphi_{mn}}\left(\frac{M_{n0}}{M_{m0}} - \frac{M_{m0}}{M_{n0}}\right).
\end{aligned}
\tag{28}
$$

Here, $\varphi_{mn} = |h_{mn}|L$ is the oscillation phase, $\omega_{mn} = 2\pi\nu_{mn}$, and $\nu_{mn} = |h_{mn}|v/2\pi$ is the first harmonic of the oscillations of the interacting m-th and n-th modes. Using the definition of the spatial beat period of the interacting modes $\rho_{mn} = 2\pi/|h_{mn}|$, the frequency ν_{mn} can be written as $\nu_{mn} = v/\rho_{mn}$. Thus, the value $1/\nu_{mn}$ can be interpreted as the characteristic displacement time of the interference pattern ρ_{mn}/v. Variations in the velocity of the inhomogeneous region lead to proportional variations in the oscillation frequency ν_{mn} without affecting the amplitude.

In Equation (25), the first term defines the stationary frequency shift in the independent mode approximation of the (the linear term in Equation (19)), while the remaining two terms arise due to mode interaction (the quadratic terms in Equation (19)). The resulting

oscillations of the phase difference $\hat{\Theta}_{mn}(t)$ include harmonics with frequencies ω_{mn}, $2\omega_{mn}$, and $3\omega_{mn}$. As in the case of independent normal modes, the interaction of modes leads to changes in the mean values of the phase difference and frequency shifts.

The phase difference $\hat{\Theta}$ between the interfering modes leads to the appearance of harmonics of the phase difference $\hat{\Theta}$. These two mechanisms differ qualitatively in that the mean phase difference is mainly determined by the parameters q_{mn} and q_{nn}, which are associated with corrections to the unperturbed values of the propagation constants. The amplitude of the oscillatory phase component is defined by the parameters q_{mn}, h_{mn}, and the interaction coefficient μ_{mn}, which governs mode coupling.

The expressions for the coefficients J_j (Equation (26)) and I_i (Equation (28)) were obtained under the approximation $|\Theta_{mn}| < 1$. To satisfy this condition, it is necessary to assume that the mode amplitudes M_{m0} and M_{n0} are of the same order, i.e., $M_{m0} \sim M_{n0}$. If one of the modes is weakly excited (for example, $M_{m0} \gg M_{n0}$), then, as $M_{n0} \to 0$, the ratio M_{m0}/M_{n0} increases indefinitely, and the small-parameter approximation is violated. In this case, the system (Equation (12)) must be solved using the initial condition $M_{n0} = 0$.

According to Equations (21) and (24), the frequency shift can be written as

$$\Omega(t) = -\frac{1}{G_{mn}}(\bar{\Theta}_{mn} + \hat{\Theta}_{mn}) = \bar{\Omega} + \hat{\Omega}(t). \tag{29}$$

As can be seen from Equations (24), (26) and (29), this formulation does not describe the frequency shift modulation of observed in numerical experiments (see Section 4). This discrepancy arises from the approximate nature of Equation (21), which is based on the Taylor expansion of the propagation constants h_m around their unperturbed values h_{m0}. For the reference value f_0, which corresponds to the position of the maximum of the field in the absence of perturbation, the linear term of the expansion is sufficient for stationary frequency shift patterns. However, for nonstationary patterns, where the position of $\Omega(t)$ varies over time, the interference of waves with closely spaced frequencies must be considered. In this case, small variations in the propagation constants produce beatings that manifest as frequency modulation.

Now, let us consider the spectrum of the interferogram of frequency shifts, which qualitatively represents the essence of the phenomenon. As shown by numerical simulations (see Section 4), the amplitudes of the spectral components $p\nu_{mn}$, (for $p = 1, 2, 3$), decrease with increasing harmonic number p, and higher harmonics have significantly smaller spectral amplitudes. The amplitude of the frequency shift at the frequency $\nu_{mn} = 0$ is determined by the stationary component $\bar{\Omega}_{mn}$. In this case, the spectral component $3\nu_{mn}$ is negligible small, so its amplitude is not visible in the figures. Therefore, we restrict our analysis to the stationary term and the first harmonic ω_{mn} of the frequency shifts (Equation (29)).

For the unperturbed waveguide model, the parameters that define the values of the coefficients J_i, and I_i, as well as the magnitude G_{12} are given in Table 3. Note that the propagation of the first ($m = 1$) and second ($n = 2$) modes was modeled. Now, if we apply the inverse Fourier transform:

$$\hat{\Omega}(\omega) = \frac{1}{2\pi}\int_{-\infty}^{\infty} \Omega(t)\, \exp(-\mathrm{i}\omega t)\, dt, \tag{30}$$

then, neglecting the edge effects associated with the incomplete entry and exit of the soliton from the track, the amplitudes of the spectral components at frequencies $\omega = 0$ and $\omega = \omega_{mn}$ can be easily found as

$$\hat{\Omega}(0) = \frac{T}{2\pi G_{mn}} J, \qquad J = J_1 + J_2, \tag{31}$$

and

$$\hat{\Omega}(\omega = \omega_{mn}) = \frac{T}{4\pi G_{mn}} I, \tag{32}$$

$$I = \sqrt{I_1^2 + I_2^2 + I_3^2 + I_4^2 + 2I_3(I_2 + I_4)\cos(\varphi_{mn}) + 2I_1(I_4 - I_2)\sin(\varphi_{mn}) + 2I_2 I_4 \cos(2\varphi_{mn})}.$$

Here, I denotes the amplitude of the harmonic of the phase difference; $T = r_0/v$ is the soliton passage time along the acoustic track. Note that the Equation (31) remains valid when edge effects are considered, if the pulse is approximated by a trapezoidal shape. In this case, the broadening width of the spectral lines at the level of 0.7 of the maximum amplitude can be estimated as

$$\delta\nu = 0.9\,\frac{v}{r_0}, \tag{33}$$

that is, to within a factor of 0.9, it is inversely proportional to the travel time T and independent of the interacting mode number. Note that the expressions for the oscillation frequencies ν_{mn} and the spectral linewidth $\Delta\nu$ were previously obtained based on numerical experiments.

Table 3. Parameters of an Unperturbed Waveguide.

Parameter	Value
h_{12}, $\times 10^{-3}\,\mathrm{m}^{-1}$	7.590
M_{01}	0.1352
M_{02}	0.1577
q_{11}, $\times 10^{-4}\,\mathrm{m}^{-2}$	1.2860
q_{22}, $\times 10^{-4}\,\mathrm{m}^{-2}$	2.8095
q_{12}, $\times 10^{-4}\,\mathrm{m}^{-2}$	2.0070
G_{12}, s	0.3391

3.4. ISW Propagates at an Angle to the Source–Receiver Path: Case $\alpha \neq 0$

Consider the propagation of an ISW with the source–receiver path at an angle of α, where $0 < \alpha < \pi/2$. As can be seen from the geometry of the problem shown in Figure 5, the problem reduces to the case of motion along the path with an angle of $\alpha = 0$, if one introduces the effective half-width $L(\alpha)$, the ISW velocity $v(\alpha)$, and the ISW traversal time along the source–receiver path $T(\alpha)$:

$$L(\alpha) = \frac{L}{\cos(\alpha)}, \qquad v(\alpha) = \frac{v}{\cos(\alpha)}, \qquad T(\alpha) = T\cos(\alpha). \tag{34}$$

Here, L, v, and T denote the corresponding quantities for $\alpha = 0$. Equations (24)–(33) remain valid in this case if the appropriate substitutions are made. However, as the angle approaches $\pi/2$, the coupled modes approximation becomes less effective. In this case, significant horizontal refraction effects caused by ISWs crossing the source–receiver path must be considered.

According to Equations (25) and (26), an increase in α leads to growth in the mean frequency shift $\bar{\Omega}$ and the adiabatic frequency shift Ω_{ad} (calculated without mode coupling), as well as a decrease in the amplitude of the oscillatory component $\hat{\Omega}(t)$. The frequency $\nu_{mn}(\alpha)$ and the width $\delta\nu(\alpha)$ of the spectral lines are given by

$$\nu_{mn}(\alpha) = \frac{\nu_{mn}}{\cos(\alpha)}, \qquad \delta\nu(\alpha) = \frac{\delta\nu}{\cos(\alpha)}. \tag{35}$$

Thus, an increase in α leads to a proportional increase by a factor of $(1/\cos(\alpha))$. At the same time, the ratio of the linewidth $\delta\nu(\alpha)$, cf. Equation (33), to the oscillation frequency $\nu_{mn}(\alpha)$ can be written as

$$\frac{\delta\nu(\alpha)}{\nu_{mn}(\alpha)} = 0.9 \cdot 2\pi\left(|h_{mn}|r_0\right)^{-1}, \tag{36}$$

which is independent of the perturbation. Furthermore, the dependence of the corresponding values on the angle α will be omitted unless it causes ambiguity.

4. Numerical Simulation Results

This section presents the results of numerical simulations of frequency-shift dynamics induced by ISWs. These simulations were performed using the parameter set summarized in Table 2. Figure 3 shows the unperturbed sound-speed profile as a function of depth. The bottom properties were specified by the density ratio of the bottom sediments to water, $\rho_b/\rho = 1.8$, and the complex refractive index $n_b = 0.82\,(1 + \mathrm{i}\,0.01)$. In the 90–120 Hz frequency band, modal groups with nearly equal amplitudes were considered, using a spectral resolution of $\delta f = 0.2$ Hz. The acoustic source and the receiver were both placed at a depth of $z_0 = 30$ m, and the horizontal propagation range was set to $r_0 = 10$ km. The soliton was represented by a squared hyperbolic secant pulse with an amplitude of $A = 15$ m, a half-width of $L = 100$ m, and a propagation velocity of $v = 1$ m/s. Particular attention was given to the coupling between the first and second acoustic modes ($m = 1$, $n = 2$) since this modal pair demonstrates the strongest interaction.

Figure 8 illustrates the temporal and spectral manifestations of ISW-induced frequency shifts when acoustic attenuation associated with bottom interaction is considered. The ISW is modeled using a squared hyperbolic secant (KdV solution) shape. Figure 8a shows that the time dependence of the frequency shift $\Omega(t)$ retains the same general structure as in the lossless case. During the ISW influence interval, the frequency shifts dependence consists of a nearly stationary mean component with superimposed oscillations. Outside this interval, the shift rapidly approaches zero. The red solid line represents the contribution without mode coupling and defines the slowly varying background level. The blue curve shows that mode coupling produces an additional oscillatory modulation around this baseline. The red dashed line shows the mean value of $\Omega(t)$, which remains close to the central level of the oscillatory response throughout the disturbed interval. Figure 8b provides an additional interpretation of these results through its spectral representation. The spectrum $\tilde{\Omega}(\nu)$ is concentrated primarily in the low-frequency range. It has a dominant peak near zero frequency and a sequence of weaker harmonics extending toward higher frequencies ν.

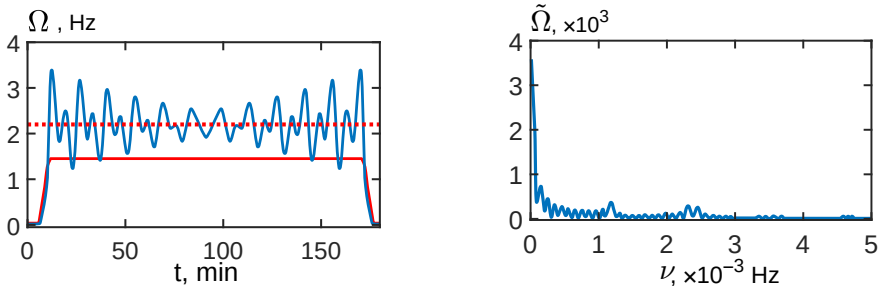


Figure 8. (**a**) Frequency shift $\Omega(t)$ due to ISW. Red dotted line—mean value of $\Omega(t)$. Red solid line—$\Omega(t)$ without mode coupling. (**b**) Spectrum $\tilde{\Omega}(\nu)$ of frequency shifts $\Omega(t)$. ISW parameters: $A = 15$ m, $L = 100$ m, $v = 1$ m/s, $\alpha = 0^\circ$. ISW is modeled by a squared hyperbolic secant (KdV solution) shape. Acoustic attenuation due to the bottom is present: $\varkappa \neq 0$.

Figure 9 shows the temporal evolution and spectral content of the ISW-induced frequency shift $\Omega(t)$ for the case in which the internal wave is represented by an approximate rectangular profile and acoustic attenuation due to bottom interaction is included. Figure 9a shows that the frequency shift remains localized within the time interval during which the inhomogeneity intersects the source–receiver path. During this time, the signal consists of a nearly steady background component and a superimposed oscillatory contribution. Outside of this interaction interval, $\Omega(t)$ rapidly drops to values close to zero, indicating that the ISW's perturbing effect on the interference structure vanishes as the wave moves away from the acoustic path. The spectral behavior shown in Figure 9b is consistent with the time-domain picture. The spectrum $\tilde{\Omega}(\nu)$ is concentrated primarily in the low-frequency range. There is a dominant contribution located near zero frequency and a set of weaker secondary maxima at higher frequencies ν. This structure reflects the coexistence of two components in $\Omega(t)$: a non-zero average level, which produces the strong low-frequency part of the spectrum, and an oscillatory modulation, which gives rise to additional spectral peaks. Therefore, the spectrum confirms that the ISW-induced frequency shift is mainly governed by slow temporal variability, while the finer oscillatory structure contributes weaker, yet still well-resolved harmonic content.

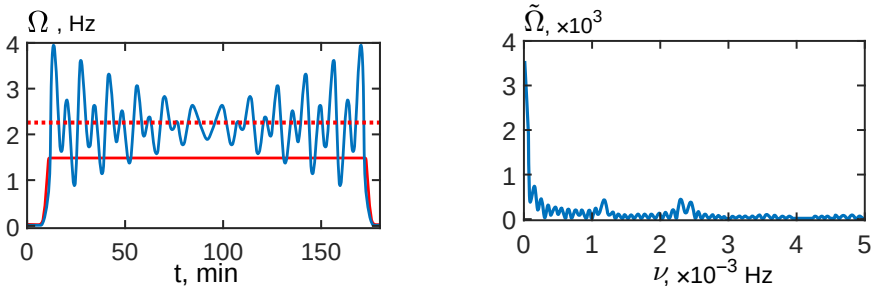


Figure 9. (**a**) Frequency shift $\Omega(t)$ due to ISW. Red dotted line—mean value of $\Omega(t)$. Red solid line—$\Omega(t)$ without mode coupling. (**b**) Spectrum $\tilde{\Omega}(\nu)$ of frequency shifts $\Omega(t)$. ISW parameters: $A = 15\,\text{m}$, $L = 100\,\text{m}$, $v = 1\,\text{m/s}$, $\alpha = 0°$. ISW is modeled by an approximate rectangular shape. Acoustic attenuation due to the bottom is present: $\varkappa \neq 0$.

An important conclusion that can be drawn from Figure 9 is that the approximate rectangular representation of the ISW retains the same main temporal and spectral signatures as the squared hyperbolic secant (KdV solution) shape. Replacing the soliton profile has little effect on the mean frequency shifts and does not alter the positions of the spectral lines. However, it leads to an increase in the amplitudes of the spectral components. For example, at the frequency $\nu = 1.174 \times 10^{-3}$ Hz, the oscillation amplitude $\tilde{\Omega}$ is equal to 341.94 for the sech^2 ISW and 416.38 for the rectangular ISW. Thus, changing the ISW shape mainly affects the spectral components amplitudes, while leaving the overall spectral structure nearly unchanged. Not only is the stationary interference pattern of frequency shifts observed, as in the case of independent modes, but also a time-dependent process associated with variations in the path difference of modes propagating from the inhomogeneity to the receiver. Additionally, the constant frequency shifts $\bar{\Omega}$ differ for coupled and independent modes.

Figure 10 shows the temporal evolution and spectrum of the ISW-induced frequency shift $\Omega(t)$ for an approximate rectangular wave profile in the absence of bottom attenuation. As seen in Figure 10a, the frequency shift is localized within the interaction interval between the inhomogeneity and the source–receiver path. During this interval, $\Omega(t)$ consists of a nearly constant mean level and an oscillatory component caused by mode coupling. Outside this interval, it rapidly approaches zero. The corresponding spectrum $\tilde{\Omega}(\nu)$, shown

in Figure 10b, is concentrated mainly in the low-frequency range and has a dominant peak near zero frequency and several weaker secondary maxima.

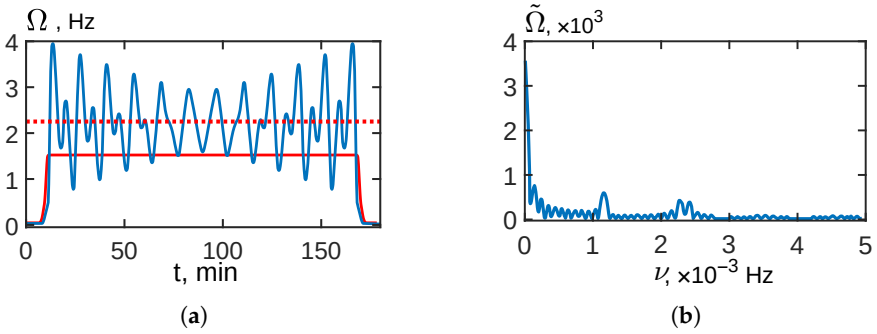
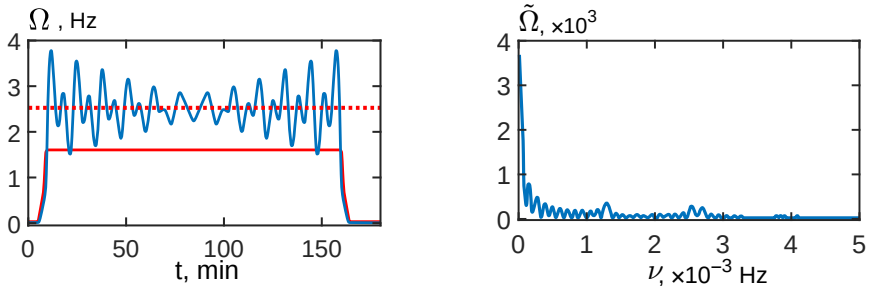


Figure 10. (**a**) Frequency shift $\Omega(t)$ due to ISW. Red dotted line—mean value of $\Omega(t)$. Red solid line—$\Omega(t)$ without mode coupling. (**b**) Spectrum $\tilde{\Omega}(\nu)$ of frequency shifts $\Omega(t)$. ISW parameters: $A = 15$ m, $L = 100$ m, $v = 1$ m/s, $\alpha = 0^\circ$. ISW is modeled by an approximate rectangular shape. Acoustic attenuation due to bottom is absent: $\varkappa = 0$.

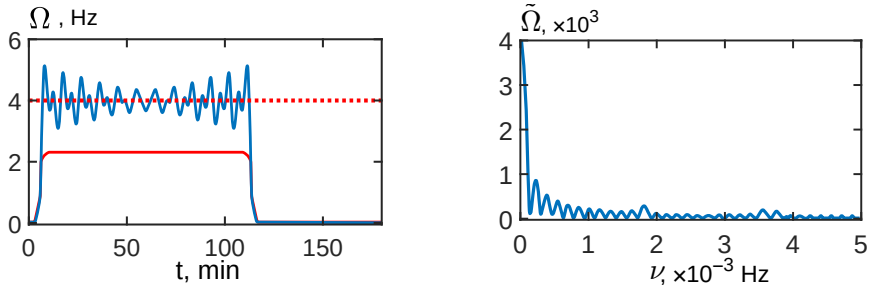
Comparing this figure with Figure 9, which includes bottom attenuation, shows that excluding bottom absorption does not substantially change the temporal behavior or the spectral structure of the frequency shifts. The mean level, the oscillation pattern, and the positions of the main spectral peaks remain nearly the same. This suggests that the influence of bottom attenuation weakly influences the frequency shifts and does not affect the main features of the ISW-induced response. For example, at $\nu = 1.174 \times 10^{-3}$ Hz, the mean frequency shift without attenuation is $\tilde{\Omega} = 577.35$, whereas with attenuation included, it is $\tilde{\Omega} = 341.94$. This demonstrates that attenuation primarily affects the magnitude of the spectral components but does not influence the frequency shift distribution pattern itself.

Figures 11–13 illustrate how the temporal and spectral characteristics of the ISW-induced frequency shift $\Omega(t)$ depend on the angle α between the wave propagation direction and the acoustic track. In all three cases include acoustic attenuation due to bottom interaction, and the ISW is modeled by the sech^2-type KdV profile. A common feature of all panels is that the frequency shift remains localized within the time interval during which the inhomogeneity affects the source–receiver path. Outside this interval $\Omega(t)$ rapidly tends to zero. The corresponding spectra $\tilde{\Omega}(\nu)$ are dominated by low-frequency components, reflecting the finite duration and relatively slow temporal modulation of the ISW-induced perturbation. Comparing of panels (a) in Figures 11–13 reveals a clear systematic influence of the angle α. As α increases from 25° to 50° and then to 75°, the duration of the disturbed interval decreases noticeably, while the mean level of the frequency shift increases. At $\alpha = 25^\circ$, the signal extends over the longest time interval and exhibits a well-developed oscillatory structure around a moderate mean level. At $\alpha = 50^\circ$, the interaction interval becomes shorter and the average value of $\Omega(t)$ grows; however, the oscillations remain clearly visible. At $\alpha = 75^\circ$, the response is strongly compressed in time and is characterized by a much larger mean frequency shift, while the oscillatory modulation is relatively weak compared to the overall level of the signal. The same tendency is evident in the spectral domain. For $\alpha = 25^\circ$, the spectrum contains a pronounced low-frequency peak, as well as a relatively rich set of secondary maxima associated with the oscillatory structure of $\Omega(t)$. As the angle increases to 50°, the spectrum remains dominated by low frequencies, though the secondary components become less significant relative to the main contribution. In the case $\alpha = 75^\circ$, the spectral energy is concentrated even more strongly in the lowest-frequency range, and the fine harmonic structure becomes much less pronounced. Thus, as α increases, the spectral pattern gradually simplifies, which is consistent with the reduced relative importance of oscillatory modulation in the time domain.



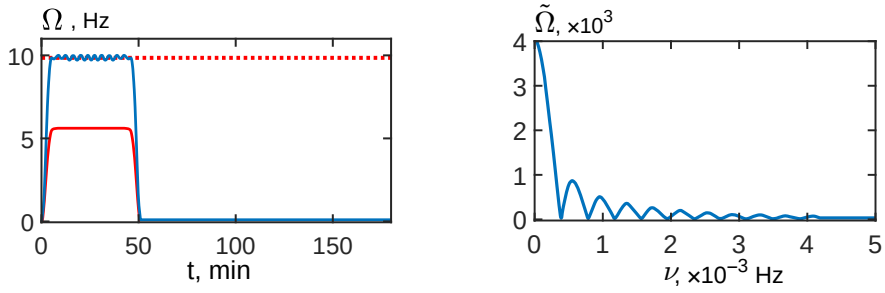
(**a**) (**b**)

Figure 11. (**a**) Frequency shift $\Omega(t)$ due to ISW. Red dotted line—mean value of $\Omega(t)$. Red solid line—$\Omega(t)$ without mode coupling. (**b**) Spectrum $\tilde{\Omega}(\nu)$ of frequency shifts $\Omega(t)$. ISW parameters: $A = 15\,\mathrm{m}$, $L = 100\,\mathrm{m}$, $v = 1\,\mathrm{m/s}$, $\alpha = 25^\circ$. ISW is modeled by a squared hyperbolic secant (KdV solution) shape. Acoustic attenuation due to the bottom is present: $\varkappa \neq 0$.



(**a**) (**b**)

Figure 12. (**a**) Frequency shift $\Omega(t)$ due to ISW. Red dotted line—mean value of $\Omega(t)$. Red solid line—$\Omega(t)$ without mode coupling. (**b**) Spectrum $\tilde{\Omega}(\nu)$ of frequency shifts $\Omega(t)$. ISW parameters: $A = 15\,\mathrm{m}$, $L = 100\,\mathrm{m}$, $v = 1\,\mathrm{m/s}$, $\alpha = 50^\circ$. ISW is modeled by a squared hyperbolic secant (KdV solution) shape. Acoustic attenuation due to the bottom is present: $\varkappa \neq 0$.



(**a**) (**b**)

Figure 13. (**a**) Frequency shift $\Omega(t)$ due to ISW. Red dotted line—mean value of $\Omega(t)$. Red solid line—$\Omega(t)$ without mode coupling. (**b**) Spectrum $\tilde{\Omega}(\nu)$ of frequency shifts $\Omega(t)$. ISW parameters: $A = 15\,\mathrm{m}$, $L = 100\,\mathrm{m}$, $v = 1\,\mathrm{m/s}$, $\alpha = 75^\circ$. ISW is modeled by a squared hyperbolic secant (KdV solution) shape. Acoustic attenuation due to the bottom is present: $\varkappa \neq 0$.

Overall, the comparative analysis of Figures 11–13 shows that the angle α is one of the key parameters controlling the ISW-induced frequency shifts. An increase in this angle yields larger mean values of $\Omega(t)$, shorter interaction times, and a stronger spectral energy concentration near zero frequency. At the same time, the contribution of mode-coupling-induced oscillations becomes less pronounced in relative terms. Therefore, the geometry of ISW propagation relative to the acoustic path significantly impacts the temporal signature and spectral content of the observed frequency-shift response.

The frequency-shift modeling results for $\alpha = 0^\circ$, 25°, 50°, and 75° are summarized in the following tables: Table 4 corresponds to Figure 8 ($\alpha = 0^\circ$); Table 5 corresponds to

Figure 11 ($\alpha = 25°$); Table 6 corresponds to Figure 12 ($\alpha = 50°$); Table 7 corresponds to Figure 13 ($\alpha = 75°$). An increase in α leads to an increase in the stationary component $\bar{\Theta}_{mn}$, a decrease in the amplitude of the oscillatory phase component, and an increase in the adiabatic frequency shift ν_{mn}, which agrees qualitatively with theoretical expectations. For $\alpha = 75°$, oscillations of the frequency shifts practically vanish, and the corresponding spectral lines are not registered against the stationary spectrum background. At the same time, the difference between the adiabatic and stationary frequency shifts Ω_{ad} and $\bar{\Omega}$ increases. Interference between the modes becomes noticeable for angles greater than $\alpha > 50°$, which is related to the coupling of two terms in Equation (19) that were used to construct the numerical model. To reduce discrepancies arising as the angle α increases, higher-order approximations must be considered, which complicates solving the inverse problem. However, this refinement has limited physical significance since the proposed theory does not consider horizontal mode refraction, which becomes noticeable for angles $\alpha > 70°$. Therefore, it can be concluded that Equation (19) is applicable only to angles $\alpha \lesssim 50°$.

Table 4. Frequency Shift Parameters: Case $\alpha = 0°$.

Parameter	Theory	Simulation
Ω_{ad}, Hz	1.348	1.452
$\bar{\Omega}$, Hz	2.075	2.188
ν_{12}, $\times 10^{-4}$ Hz	1.209	1.174
$\delta\nu$, $\times 10^{-4}$ Hz	0.899	0.909
Spectral amplitude at the frequency ν_{12}	605.33	341.94

Table 5. Frequency Shift Parameters: Case $\alpha = 25°$.

Parameter	Theory	Simulation
Ω_{ad}, Hz	1.487	1.602
$\bar{\Omega}$, Hz	2.468	2.524
ν_{12}, $\times 10^{-4}$ Hz	1.333	1.295
$\delta\nu$, $\times 10^{-4}$ Hz	0.992	1.018
Spectral amplitude at the frequency ν_{12}	642.65	331.22

Table 6. Frequency Shift Parameters: Case $\alpha = 50°$.

Parameter	Theory	Simulation
Ω_{ad}, Hz	2.097	2.286
$\bar{\Omega}$, Hz	4.904	3.981
ν_{12}, $\times 10^{-4}$ Hz	1.880	1.810
$\delta\nu$, $\times 10^{-4}$ Hz	1.556	1.363
Spectral amplitude at the frequency ν_{12}	728.18	264.19

Table 7. Frequency Shift Parameters: Case $\alpha = 75°$.

Parameter	Theory	Simulation
Ω_{ad}, Hz	5.207	5.531
$\bar{\Omega}$, Hz	51.178	9.737
ν_{12}, $\times 10^{-4}$ Hz	—	—
$\delta\nu$, $\times 10^{-4}$ Hz	—	—
Spectral amplitude at the frequency ν_{12}	—	—

5. Internal Soliton Wave Parameters Estimation

The analytical and numerical results presented in Sections 3 and 4 show that mode coupling induced by ISW generates distinct and stable features in the frequency shift spectrum. These features are strongly influenced by soliton parameters, such as propagation direction, velocity, and effective amplitude, as well as by the modal structure of the acoustic field. Furthermore, we demonstrated that these spectral characteristics can serve as informative indicators of internal wave dynamics. To illustrate the potential feasibility of retrieving key ISW parameters from observed frequency shifts, we present a numerical experiment. This numerical experiment is illustrated in Figure 14. Two acoustic propagation paths originate from a common source S and terminate at receivers Q_1 ($\alpha_1 = 40^\circ$) and Q_2 ($\alpha_2 = 20^\circ$), which are positioned so that the angle between the paths is $\varphi = 20^\circ$. The length of each path is $r_0 = 10$ km. We assume that the characteristics of the unperturbed acoustic waveguide are known (see Table 2).

The ISW intersects both propagation paths at angles α_1 and α_2. The simulation uses the following soliton parameters: amplitude $A = 15$ m, half-width $L = 100$ m, propagation velocity $v = 1$ m/s, and intersection angles $\alpha_1 = 40^\circ$ and $\alpha_2 = 20^\circ$. The goal is to determine the soliton parameters and its direction of motion based on the frequency shifts obtained numerically, which are presented in Figures 15 and 16 for the first and second paths, respectively.

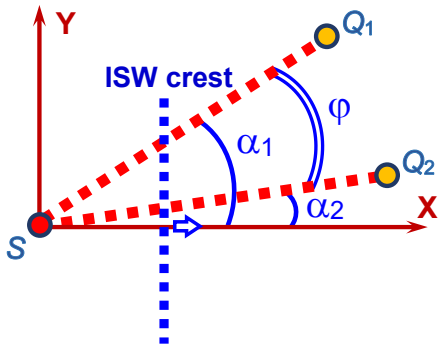


Figure 14. Geometry of the problem: S—source; Q_1—first receiver; Q_2—second receiver; red dashed lines—$S-Q_1$ and $S-Q_2$ paths; blue dashed line—ISW crest; blue arrow—ISW velocity vector **v**; $\alpha_1 = 40^\circ$ angle between $S-Q_1$ path and X-axis; $\alpha_2 = 20^\circ$ angle between $S-Q_2$ path and X-axis; φ angle between $S-Q_1$ and $S-Q_2$ paths.

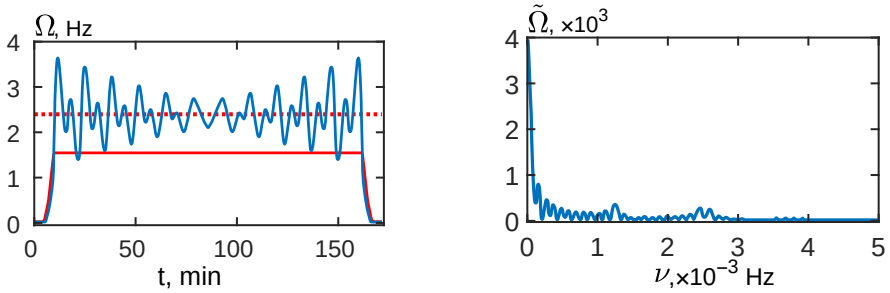
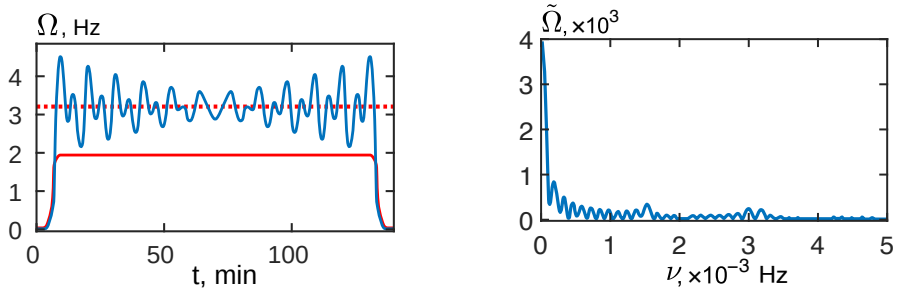


Figure 15. (**a**) Frequency shift $\Omega(t)$ due to ISW. Red dotted line—mean value of $\Omega(t)$. Red solid line—$\Omega(t)$ without mode coupling. (**b**) Spectrum $\tilde{\Omega}(\nu)$ of frequency shifts $\Omega(t)$. ISW parameters: $A = 15$ m, $L = 100$ m, $v = 1$ m/s, $\alpha_1 = 40^\circ$. ISW is modeled by a squared hyperbolic secant (KdV solution) shape. Acoustic attenuation due to bottom is present: $\varkappa \neq 0$. Results corresponds to $S-Q_1$ path.



(**a**) (**b**)

Figure 16. (**a**) Frequency shift $\Omega(t)$ due to ISW. Red dotted line—mean value of $\Omega(t)$. Red solid line—$\Omega(t)$ without mode coupling. (**b**) Spectrum $\tilde{\Omega}(\nu)$ of frequency shifts $\Omega(t)$. ISW parameters: $A = 15\,\text{m}$, $L = 100\,\text{m}$, $v = 1\,\text{m/s}$, $\alpha_2 = 20^\circ$. ISW is modeled by a squared hyperbolic secant (KdV solution) shape. Acoustic attenuation due to bottom is present: $\varkappa \neq 0$. Results corresponds to $S - Q_2$ path.

The values of the frequency-shift parameters obtained in the numerical experiment are summarized in Tables 8 and 9. The procedure used to reconstruct the soliton parameters is outlined below. By measuring the oscillation frequencies $\nu_{12}(\alpha_1)$ and $\nu_{12}(\alpha_2)$ along the two acoustic paths, and taking into account the geometric relation between the angles, $\alpha_1 = \alpha_2 + \varphi$, an equation for determining α_2 can be obtained:

$$\tan(\alpha_1) = \frac{\gamma\cos(\varphi) - 1}{\gamma\sin(\varphi)}, \tag{37}$$

where $\gamma = \nu_{12}(\alpha_1)/\nu_{12}(\alpha_2)$. Using Equation (19), the soliton's propagation velocity can be estimated from measurements of the soliton propagation direction and the spectral line width recorded on one of the acoustic paths. This estimate can be written as

$$\nu = 1.1\, r_0\, \delta\nu(\alpha_{1,2})\, \cos(\alpha_{1,2}). \tag{38}$$

According to the parameters listed in Table 3, the contributions of the terms J_3 and J_4 in Equation (26) are small and can be neglected when evaluating the constant component $\bar{\Theta}_{mn}$ defined in Equation (25). Therefore, determining the soliton pulse parameter AL from measurements of the mean frequency shift $\Omega(\alpha_{1,2})$ reduces to solving a cubic equation. The average frequency shift corresponding to the angles $\alpha_{1,2}$ can be written in the form:

$$\bar{\Omega}(\alpha_{1,2}) = -\frac{1}{G_{12}}\left[\frac{2AL}{\cos(\alpha_{1,2})}(q_{11} - q_{22}) + \frac{4(AL)^3}{\cos^3(\alpha_{1,2})}(q_{11}^3 - q_{22}^3)\right]. \tag{39}$$

The difference in the propagation constants $|h_{12}|$ of the unperturbed waveguide can be obtained from Equation (36) using the available measurement data. This approach accounts for potential discrepancies between the actual and assumed environmental parameters during the experiment. At the same time, the problem of separating the factors contained in the parameter AL remains unresolved.

Table 8. Frequency Shift Parameters: First Path.

Parameter	First Path
ν_{12}, Hz	1.2650×10^{-3}
$\delta\nu$, Hz	9.8152×10^{-5}
$\bar{\Omega}$, Hz	2.3959

Table 9. Frequency Shift Parameters: Second Path.

Parameter	Second Path
ν_{12}, Hz	1.5376×10^{-3}
$\delta\nu$, Hz	1.1724×10^{-4}
$\bar{\Omega}$, Hz	3.1910

The results of the soliton parameter reconstruction are summarized in Table 10. These data indicate that the estimates obtained from the two propagation paths are consistent with the model parameters. The values reconstructed using the two acoustic paths are highly aligned, demonstrating the stability and reliability of the estimates. The numerical simulation results presented here illustrate the feasibility of retrieving key ISW parameters from observed frequency shifts. However, rigorously justifying this inverse approach requires detailed validation, including error quantification, sensitivity analysis, and benchmarking against established inversion techniques. The authors plan to address these aspects in a subsequent study.

Table 10. ISW Parameters Estimation.

Parameter	Model Values	First-Path Data	Second-Path Data
v, m/s	1	1.013	1.031
α_1/α_2, deg	$40^\circ/20^\circ$	$38^\circ 54'$	$18^\circ 54'$
AL, m^2	1500	1447	1509
$\lvert h_{12}\rvert$, m^{-1}	7.590×10^{-3}	7.413×10^{-3}	7.284×10^{-3}

6. Conclusions

The paper presents a theoretical framework for describing frequency shifts in broadband acoustic field interference structures caused by ISW in shallow water. Using the well-known coupled mode approach, we analyzed the influence of ISW-induced perturbations on the frequency shifts of interference maxima in detail. We placed particular emphasis on the relationship between observable spectral signatures and ISW parameters.

Within the weak coupling approximation, the following analytical expressions are derived:

- M_m—*mode amplitude variations;*
- Θ_m—*mode phase variations;*
- Ω_{mn}—*frequency shifts;*
- ν_{mn}—*peak frequency in spectrum of frequency shift variations;*
- $\delta\nu_{mn}$—*peak width in spectrum of frequency shift variations.*

These analytical results have been thoroughly evaluated through numerical simulations conducted under realistic ocean conditions. This includes conditions where the weak coupling approximation is no longer applicable.

These analytical and numerical results demonstrate that soliton-induced mode coupling produces distinct and stable signatures of ISWs in the frequency shift spectrum. These signatures are strongly influenced by key soliton parameters, such as propagation direction, velocity, and effective amplitude, as well as the modal structure of the acoustic field. Together, these findings provide a consistent, physically grounded description of frequency shift phenomena in shallow water in the presence of ISW. Furthermore, it is demonstrated that these spectral features can serve as informative indicators of internal wave dynamics. The study's findings suggest the feasibility of estimating key soliton parameters from frequency shifts, a conclusion supported by the paper's numerical simulations. This provides a basis for interpreting acoustic observations in terms of underlying environmental processes. Overall, the results underscore the potential of frequency shift

analysis as an effective, robust tool for the remote sensing and monitoring of internal wave dynamics in ocean acoustics.

Nevertheless, rigorously assessing the proposed inverse approach requires detailed validation, including quantitative error analysis, sensitivity studies, and benchmarking against established inversion methods. The authors plan to address these issues in a future study.

7. Future Works

The present study establishes the fundamental feasibility of inferring ISW parameters from frequency shift measurements. However, a thorough evaluation of the proposed inverse methodology is needed, including quantifying systematic errors, conducting sensitivity analysis, and comparing it with established inversion approaches. These aspects will be investigated in detail in future studies. Subsequent research will focus on thoroughly validating the method using numerical simulations and experimental data. Specifically, the method will be tested for retrieving soliton parameters from frequency shifts of interference maxima using datasets such as SWARM'95, ASIAEX'01, SHALLOW WATER'06 and others [38,83–86].

Author Contributions: Supervision and project administration, M.E. and S.P.; conceptualization and methodology, V.K. and S.P.; software, S.T. and A.P.; validation, M.E. and V.K.; formal analysis, M.E. and S.P.; writing—original draft preparation, M.E. and S.P.; writing—review and editing, M.E. and S.P. All authors have read and agreed to the published version of the manuscript.

Funding: This work was supported in part by the Ministry of Education and Science of the Russian Federation through Project No. FZGU-2026-0008. The numerical simulation of the frequency shifts was supported by a grant from the Russian Science Foundation No. 23-61-10024, https://rscf.ru/project/23-61-10024/ (accessed on 23 March 2026).

Data Availability Statement: The original data used in the study are openly available. The waveguide model used in the simulation is based on parameters from the SWARM'95 experiments [37,38].

Conflicts of Interest: The authors declare no conflicts of interest.

Abbreviations

The following abbreviations are used in this manuscript:

ISP	interferometric signal processing
HSP	holographic signal processing
ISW	internal soliton wave
FS	frequency shift
MFP	matched field processing
3DHE	3D Helmholtz Equation model
3DPE	3D Parabolic Equation model
3DR	3D Ray-based model
VMMPE	Vertical Modes and 2D Modal Parabolic Equation model
VCMHR	Vertical Coupled Modes with Horizontal Rays model

References

1. Weston, D.; Stevens, K. Interference of wide-band sound in shallow water. *J. Sound Vib.* **1972**, *21*, 57–64. [CrossRef]
2. Chuprov, S. Interference structure of a sound field in a layered ocean. In *Ocean Acoustics, Current Status*; Brekhovskikh, L.M., Andreyeva, I.B., Eds.; Nauka: Moscow, Russia, 1982; pp. 71–91.
3. D'Spain, G.L.; Kuperman, W.A. Application of waveguide invariants to analysis of spectrograms from shallow water environments that vary in range and azimuth. *J. Acoust. Soc. Am.* **1999**, *106*, 2454–2468. [CrossRef]
4. Cockrell, K.L.; Schmidt, H. A relationship between the waveguide invariant and wavenumber integration. *J. Acoust. Soc. Am.* **2010**, *128*, EL63–EL68. [CrossRef]

5. Cockrell, K.L.; Schmidt, H. A modal Wentzel–Kramers–Brillouin approach to calculating the waveguide invariant for non-ideal waveguides. *J. Acoust. Soc. Am.* **2011**, *130*, 72–83. [CrossRef]
6. Harrison, C.H. The relation between the waveguide invariant, multipath impulse response, and ray cycles. *J. Acoust. Soc. Am.* **2011**, *129*, 2863–2877. [CrossRef] [PubMed]
7. Sell, A.W.; Culver, R.L. Waveguide invariant analysis for modeling time-frequency striations in a range-dependent environment. *J. Acoust. Soc. Am.* **2011**, *130*, EL316–EL322. [CrossRef]
8. Song, H.C.; Cho, C. The relation between the waveguide invariant and array invariant. *J. Acoust. Soc. Am.* **2015**, *138*, 899–903. [CrossRef] [PubMed]
9. Zhao, Z.D.; Wu, J.R.; Shang, E.C. How the thermocline affects the value of the waveguide invariant in a shallow-water waveguide. *J. Acoust. Soc. Am.* **2015**, *138*, 223–231. [CrossRef]
10. Weng, J.; Li, F.; Guo, Y. The sound field frequency-range interference patterns in deep water: Theory and experiment. *Acta Acust.* **2016**, *41*, 330–342.
11. Turgut, A.; Fialkowski, L.T.; Schindall, J.A. Measured depth-dependence of waveguide invariant in shallow water with a summer profile. *J. Acoust. Soc. Am. Express Lett.* **2016**, *139*, EL184–EL189. [CrossRef]
12. Song, W.; Wang, N.; Gao, D.; Wang, H.; Hu, T.; Guo, S. The influence of mode coupling on waveguide invariant. *J. Acoust. Soc. Am.* **2017**, *142*, 1848–1857. [CrossRef]
13. Emmetière, R.; Bonnel, J.; Géhant, M.; Cristol, X.; Chonavel, T. Understanding deep-water striation patterns and predicting the waveguide invariant as a distribution depending on range and depth. *J. Acoust. Soc. Am.* **2018**, *143*, 3444–3454. [CrossRef]
14. Ianniello, J. Recent developments in sonar signal processing. *IEEE Signal Proc. Mag.* **1998**, *15*, 27–40.
15. Thode, A.M. Source ranging with minimal environmental information using a virtual receiver and waveguide invariant theory. *J. Acoust. Soc. Am.* **2000**, *108*, 1582–1594. [CrossRef] [PubMed]
16. Kuperman, W.A.; D'Spain, G.L. *Ocean Acoustic Interference Phenomena and Signal Processing*; American Institute of Physics: College Park, MD, USA, 2002; Volume 621.
17. Rouseff, D.; Spindel, R.C. Modeling the waveguide invariant as a distribution. *AIP Conf. Proc. Amer. Inst. Phys.* **2002**, *621*, 137–150.
18. Baggeroer, A.B. Estimation of the distribution of the interference invariant with seismic streamers. *AIP Conf. Proc. Amer. Inst. Phys.* **2002**, *621*, 151–170.
19. Yang, T. Beam intensity striations and applications. *J. Acoust. Soc. Am.* **2003**, *113*, 1342–1352. [CrossRef] [PubMed]
20. Heaney, K.D. Rapid geoacoustic characterization using a surface ship of opportunity. *IEEE J. Ocean. Eng.* **2004**, *29*, 88–99. [CrossRef]
21. Cockrell, K.L.; Schmidt, H. Robust passive range estimation using the waveguide invariant. *J. Acoust. Soc. Am.* **2010**, *127*, 2780–2789. [CrossRef]
22. Rouseff, D.; Zurk, L.M. Striation-based beam forming for estimating the waveguide invariant with passive sonar. *J. Acoust. Soc. Am. Express Lett.* **2011**, *130*, 76–81. [CrossRef]
23. Emmetiere, R.; Bonnel, J.; Cristol, X.; Gehant, M.; Chonavel, T. Passive source depth discrimination in deep-water. *IEEE J. Select. Top. Signal Process.* **2019**, *13*, 185–197.
24. Kuznetsov, G.N.; Kuzkin, V.M.; Pereselkov, S.A. Spectrogram and localization of a sound source in a shallow sea. *Acoust. Phys.* **2017**, *63*, 449–461.
25. Ehrhardt, M.; Pereselkov, S.A.; Kuz'kin, V.M.; Kaznacheev, I.; Rybyanets, P. Experimental observation and theoretical analysis of the low-frequency source interferogram and hologram in shallow water. *J. Sound Vibr.* **2023**, *544*, 117388. [CrossRef]
26. Pereselkov, S.; Kuz'kin, V.; Ehrhardt, M.; Tkachenko, S.; Pereselkov, A.; Ladykin, N. Application of Fractional Fourier Transform to Hologram Formation of a Moving Acoustic Source. *Fractal Fract.* **2025**, *9*, 715. [CrossRef]
27. Pereselkov, S.; Kuz'kin, V.; Ehrhardt, M.; Tkachenko, S.; Rybyanets, P.; Ladykin, N. Use of Interference Patterns to Control Sound Field Focusing in Shallow Water. *J. Mar. Sci. Eng.* **2023**, *11*, 559. [CrossRef]
28. Baggeroer, A.B.; Kuperman, W.A.; Mikhalevsky, P.N. An overview of matched field methods in ocean acoustics. *IEEE J. Ocean. Eng.* **1993**, *18*, 401–424. [CrossRef]
29. Tolstoy, A. *Matched Field Processing for Underwater Acoustics*; World Scientific: Singapore, 1993; Volume 18, pp. 1–212.
30. Jackson, D.R.; Ewart, T.E. The effect of internal waves on matched-field processing. *J. Acoust. Soc. Am.* **1994**, *96*, 2945–2955. [CrossRef]
31. Baggeroer, A.B.; Kuperman, W.A.; Schmidt, H. Matched field processing: Source localization in correlated noise as an optimum parameter estimation problem. *J. Acoust. Soc. Am.* **1998**, *83*, 571–587. [CrossRef]
32. Baggeroer, A.B. Why did applications of MFP fail, or did we not understand how to apply MFP? In *Proceedings of the 1st International Conference and Exhibition on Underwater Acoustics, Corfu Island, Greece, 23–28 June 2013*; Papadakis, J.S., Bjorno, L., Eds.; Foundation for Research & Technology-Hellas (FORTH): Heraklion, Greece, 2013; pp. 41–49.
33. Kuz'kin, V.M.; Pereselkov, S.A.; Zvyagin, V.G.; Malykhin, A.Y.; Prosovetskiy, D.Y. Intense internal waves and their manifestation in interference patterns of received signals on oceanic shelf. *Phys. Wave Phenom.* **2018**, *26*, 160–167. [CrossRef]

34. Badiey, M.; Kuz'kin, V.M.; Lyakhov, G.A.; Pereselkov, S.A.; Prosovetskiy, D.Y.; Tkachenko, S.A. Intense internal waves and their manifestation in the interference patterns of received signals on oceanic shelf. Part II. *Phys. Wave Phenom.* **2019**, *27*, 313–319. [CrossRef]
35. Kaznacheeva, E.S.; Kuz'kin, V.M.; Pereselkov, S.A. Interferometric processing of hydroacoustic information in the presence of intense internal waves. *Phys. Wave Phenom.* **2021**, *29*, 278–284. [CrossRef]
36. Badiey, M.; Kuz'kin, V.M.; Pereselkov, C.A.; Ladykin, N.V.; Malykhin, A.Y.; Tkachenko, S.A. Robustness of holographic processing of hydroacoustic signals in the presence of intense internal waves. *Phys. Wave Phenom.* **2023**, *31*, 346–354. [CrossRef]
37. Badiey, M.; SWARM'95 group. *Ocean Acoustic Experiments in Support of Shallow Water Acoustic Remote Measurements (SWARM)*; Cruise Report; University of Delaware: Newark, DE, USA, 1995; p. 72.
38. Apel, J.R.; Badiey, M.; Chiu, C.-S.; Finette, S.; Headrick, R.H.; Kemp, J.; Lynch, J.F.; Newhall, A.E.; Orr, M.H.; Pasewark, B.H.; et al. An overview of the SWARM 1995 shallow-water internal wave acoustic scattering experiment. *IEEE J. Ocean. Eng.* **1997**, *22*, 465–500. [CrossRef]
39. Badiey, M.; Katsnelson, B.G.; Lynch, J.F.; Pereselkov, S.A.; Siegmann, W. Measurement and modeling of three-dimensional sound intensity variations due to shallow-water internal waves. *J. Acoust. Soc. Am.* **2005**, *117*, 613–625. [CrossRef] [PubMed]
40. Serebryany, A.N. Manifestation of the properties of solitons in internal waves on the shelf. *Izv. Acad. Sci. USSR Phys. Atmos. Ocean* **1993**, *29*, 285–293.
41. Ostrovsky, L.A.; Stepanyants, Y.A. Do internal solitons exist in the ocean? *Rev. Geophys.* **1989**, *27*, 293–310. [CrossRef]
42. Konyaev, K.V.; Sabinin, K.D. *Waves Inside the Ocean*; Gidromet. Publication: St. Petersburg, Russia, 1992; 271p.
43. Pereselkov, S.; Kuz'kin, V.; Ehrhardt, M.; Tkachenko, S.; Rybyanets, P.; Ladykin, N. Three-Dimensional Modeling of Sound Field Holograms of a Moving Source in the Presence of Internal Waves Causing Horizontal Refraction. *J. Mar. Sci. Eng.* **2023**, *11*, 1922. [CrossRef]
44. Pereselkov, S.; Kuz'kin, V.; Ehrhardt, M.; Tkachenko, S.; Pereselkov, A.; Ladykin, N. Influence of Intense Internal Waves Traveling Along an Acoustic Path on Source Holographic Reconstruction in Shallow Water. *J. Mar. Sci. Eng.* **2025**, *13*, 1409. [CrossRef]
45. Kuz'kin, V.M. Frequency shifts of the sound field interference pattern in a shallow sea. *Acoust. Phys.* **1999**, *45*, 224–229.
46. Kuz'kin, V.M.; Pereselkov, S.A.; Oppengeim, V.D. The sensitivity of monitoring by measuring the frequency shifts of the sound field interference pattern. *Acoust. Phys.* **2008**, *54*, 224–227. [CrossRef]
47. Kuz'kin, V.M.; Pereselkov, S.A. Frequency shifts of the spatial interference structure of the sound field in a shallow sea. *Acoust. Phys.* **2008**, *54*, 375–381. [CrossRef]
48. Kuz'kin, V.M.; Pereselkov, S.A. Methods of measuring frequency shifts in the interference structure of the sound field in oceanic waveguides. *Acoust. Phys.* **2010**, *56*, 514–524. [CrossRef]
49. Kuz'kin, V.M.; Pereselkov, S.A.; Lyakhov, G.A. Method for measuring the frequency shifts of interference maxima in monitoring of dispersive media. *Phys. Wave Phenom.* **2010**, *18*, 196–203. [CrossRef]
50. Lin, Y.-T.; Porter, M.B.; Sturm, F.; Isakson, M.J.; Chiu, C.-S. Introduction to the special issue on three-dimensional underwater acoustics. *J. Acoust. Soc. Am.* **2019**, *146*, 1855–1857. [CrossRef] [PubMed]
51. Liu, W.; Zhang, L.; Wang, W.; Wang, Y.; Ma, S.; Cheng, X.; Xiao, W. A three-dimensional finite difference model for ocean acoustic propagation and benchmarking for topographic effects. *J. Acoust. Soc. Am.* **2021**, *150*, 1140–1156. [CrossRef] [PubMed]
52. Tu, H.; Wang, Y.; Liu, W.; Yang, C.; Qin, J.; Ma, S.; Wang, X. Application of a Spectral Method to Simulate Quasi-Three-Dimensional Underwater Acoustic Fields. *J. Sound Vibr.* **2023**, *545*, 117421. [CrossRef]
53. Larsson, E.; Abrahamsson, L. Helmholtz and parabolic equation solutions to a benchmark problem in ocean acoustics. *J. Acoust. Soc. Am.* **2003**, *113*, 2446–2454. [CrossRef]
54. Smith, K.B.; Tappert, F.D. UMPE: The University of Miami Parabolic Equation Model. Version 1.1 "MPL Technical Memorandum 432". 1993; p. 96. Available online: https://oalib-acoustics.org/website_resources/PE/UMPE/UMPE.pdf (accessed on 25 April 2026).
55. Tappert, F.D. The parabolic approximation method. In *Wave Propagation and Underwater Acoustics*; Keller, J.B., Papadakis, J.S., Eds.; Lecture Notes in Physics; Springer: New York, NY, USA, 1977; Volume 70, Chapter 5, pp. 224–287.
56. Lin, Y.-T. Three-dimensional boundary fitted parabolic-equation model of underwater sound propagation. *J. Acoust. Soc. Am.* **2019**, *146*, 2058–2067. [CrossRef] [PubMed]
57. Heaney, K.D.; Campbell, R.L. Three-dimensional parabolic equation modeling of mesoscale eddy deflection. *J. Acoust. Soc. Am.* **2016**, *139*, 918–926. [CrossRef]
58. Ivansson, S. Local accuracy of cross-term corrections of three-dimensional parabolic-equation models. *J. Acoust. Soc. Am.* **2019**, *146*, 2030–2040. [CrossRef]
59. Lee, K.; Seong, W.; Na, Y. Three-dimensional Cartesian parabolic equation model with higher-order cross-terms using operator splitting, rational filtering, and split-step Padé algorithm. *J. Acoust. Soc. Am.* **2019**, *146*, 2041–2049. [CrossRef]
60. Lee, K.; Seong, W.; Na, Y. Split-step Padé solver for three dimensional Cartesian acoustic parabolic equation in stair-step representation of ocean environment. *J. Acoust. Soc. Am.* **2019**, *146*, 2050–2057. [CrossRef]

61. Porter, M.B. Beam tracing for two- and three-dimensional problems in ocean acoustics. *J. Acoust. Soc. Am.* **2019**, *146*, 2016–2029. [CrossRef] [PubMed]
62. Porter, M.B. *Bellhop3d User Guide*; Heat, Light, and Sound Research, Inc.: La Jolla, CA, USA, 2016.
63. Jensen, F.B.; Kuperman, W.A.; Porter, M.B.; Schmidt, H.; Tolstoy, A. *Computational Ocean Acoustics*; Springer: Berlin/Heidelberg, Germany, 2011.
64. Katsnelson, B.G.; Pereselkov, S.A. Low-frequency horizontal acoustic refraction caused by internal wave solitons in a shallow sea. *Acoust. Phys.* **2000**, *46*, 684–691. [CrossRef]
65. Collins, M.D. The adiabatic mode parabolic equation. *J. Acoust. Soc. Am.* **1993**, *94*, 2269–2278. [CrossRef]
66. Trofimov, M.Y.; Kozitskiy, S.; Zakharenko, A. A mode parabolic equation method in the case of the resonant mode interaction. *Wave Motion* **2015**, *58*, 42–52. [CrossRef]
67. Petrov, P.S.; Sturm, F. An explicit analytical solution for sound propagation in a three-dimensional penetrable wedge with small apex angle. *J. Acoust. Soc. Am.* **2016**, *139*, 1343–1352. [CrossRef]
68. Kohler, W.; Papanicolaou, G.C. Wave propagation in a randomly inhomogeneous ocean. In *Wave Propagation and Underwater Acoustics*; Keller, J.B., Papadakis, J.S., Eds.; Lecture Notes in Physics; Springer: Berlin/Heidelberg, Germany, 1977; Volume 70, pp. 153–223.
69. Dozier, L.B.; Tappert, F.D. Mode coupling—Surface roughness. *J. Acoust. Soc. Am.* **1978**, *63*, 353–365. [CrossRef]
70. Dozier, L.B.; Tappert, F.D. Mode coupling—Bottom roughness. *J. Acoust. Soc. Am.* **1978**, *63*, 365–370.
71. Fawcett, J.A. Coupled-mode equation refinements. *J. Acoust. Soc. Am.* **1992**, *91*, 2052–2061.
72. Trofimov, M.; Kozitskiy, S.; Zakharenko, A.; Petrov, P. Formal Derivations of Mode Coupling Equations in Underwater Acoustics: How the Method of Multiple Scales Results in an Expansion over Eigenfunctions and the Vectorized WKBJ Solution for the Amplitudes. *J. Mar. Sci. Eng.* **2023**, *11*, 797–812. [CrossRef]
73. Colosi, J.A.; Flatté, S.M. Mode coupling by internal waves. *J. Acoust. Soc. Am.* **1996**, *100*, 3607–3620. [CrossRef]
74. Zhou, J.X.; Zhang, X.Z.; Rogers, P.H. Resonant interaction of sound wave with internal solitons in the coastal ocean. *J. Acoust. Soc. Am.* **1991**, *90*, 2042–2054. [CrossRef]
75. Preisig, J.C.; Duda, T.F. Coupled acoustic mode propagation through continental-shelf internal solitary waves. *IEEE J. Ocean. Eng.* **1997**, *22*, 256–269. [CrossRef]
76. Duda, T.F.; Preisig, J.C. A modeling study of acoustic propagation through moving shallow-water nonlinear wave packets. *IEEE J. Ocean. Eng.* **1999**, *24*, 16–32. [CrossRef]
77. Duda, T.F. Acoustic mode coupling by nonlinear internal wave packets in a shelf break front area. *IEEE J. Ocean. Eng.* **2004**, *29*, 118–125. [CrossRef]
78. Higham, C.J.; Tindle, C.T. Coupled perturbed modes and internal solitary waves. *J. Acoust. Soc. Am.* **2003**, *113*, 2515–2522. [CrossRef]
79. Feng, L.; Goff, J.A.; Yang, B. Nonlinear internal-wave interaction. *J. Acoust. Soc. Am.* **2004**, *116*, 2300–2310.
80. Colosi, J.A. Acoustic mode coupling induced by shallow water nonlinear internal waves: Sensitivity to environmental conditions and space–time scales of internal waves. *J. Acoust. Soc. Am.* **2008**, *124*, 1452–1464. [CrossRef]
81. Yang, T.C. Acoustic mode coupling induced by nonlinear internal waves: Evaluation of the mode coupling matrices and applications. *J. Acoust. Soc. Am.* **2014**, *135*, 610–625. [CrossRef]
82. Brekhovskikh, L.M.; Lysanov, Y.P. *Fundamentals of Ocean Acoustics*; Springer: Berlin/Heidelberg, Germany, 2013.
83. Tang, D.; Moum, J.N.; Lynch, J.F.; Abbot, P.; Chapman, R.; Dahl, P.H.; Duda, T.F.; Gawarkiewicz, G.; Glenn, S.; Goff, J.A.; et al. Shallow Water '06: A joint acoustic propagation/nonlinear internal wave physics experiment. *Oceanography* **2007**, *20*, 156–167. [CrossRef]
84. Wei, R.-C.; Chen, C.-F.; Chan, H.-C. Initial study of ambient noise modeling for the 2001 ASIAEX South China Sea experiment. *J. Acoust. Soc. Am.* **2004**, *115*, 2508–2509.
85. Lynch, J.F.; Ramp, S.R.; Dahl, P.H.; Chiu, C.-S. Overview of results from the Asian Seas International Acoustics Experiment (ASIAEX) in the South China Sea 2001. *IEEE J. Ocean. Eng.* **2004**, *29*, 1067–1074. [CrossRef]
86. Headrick, R.H.; Lynch, J.F.; Kemp, J.N.; Newhall, A.E.; von der Heydt, K.; Apel, J.; Badiey, M.; Chiu, C.-S.; Finette, S.; Orr, M.; et al. Acoustic normal-mode fluctuation statistics in the 1995 SWARM internal-wave scattering experiment. *J. Acoust. Soc. Am.* **2000**, *107*, 201–220. [CrossRef]

Disclaimer/Publisher's Note: The statements, opinions and data contained in all publications are solely those of the individual author(s) and contributor(s) and not of MDPI and/or the editor(s). MDPI and/or the editor(s) disclaim responsibility for any injury to people or property resulting from any ideas, methods, instructions or products referred to in the content.